Numerical Analysis of Airflow and Output of Solar Chimney Power Plants

Christopher Allen Stockinger

Thesis submitted to the faculty of the Virginia Polytechnic Institute and State University in partial fulfillment of the requirements for the degree of

Master of Science

In

Mechanical Engineering

Francine Battaglia, Chair

Amrinder Nain

Zhiting Tian

04/27/2016

Blacksburg, VA

Keywords: Buoyancy-Driven Flow, Computational Fluid Dynamics, Natural Convection, Power Plant, Solar Chimney, Solar Updraft Tower

Numerical Analysis of Airflow and Output of Solar Chimney Power Plants

Christopher Allen Stockinger

Abstract

Computational fluid dynamics was used to simulate solar chimney power plants and investigate modeling techniques and expected energy output from the system. The solar chimney consists of three primary parts: a collector made of a transparent material such as glass, a tower made of concrete located at the center of the collector, and a turbine that is typically placed at the bottom of the tower. The collector absorbs solar radiation and heats the air below, whereby air flows inward towards the tower. As air exits at the top of the tower, more air is drawn below the collector repeating the process. The turbine converts pressure within the flow into power. The study investigated three validation cases to numerically model the system properly. Modeling the turbine as a pressure drop allows for the turbine power output to be calculated while not physically modeling the turbine. The numerical model was used to investigate air properties, such as velocity, temperature, and pressure. The results supported the claim that increasing the energy into the system increased both the velocities and temperatures. Also, increasing the turbine pressure drop decreases the velocities and increases the temperatures within the system. In addition to the numerical model, analytical models representing the vertical velocity without the turbine and the maximum power output from a specific chimney were used to investigate the effects on the flow when varying the geometry. Increasing the height of the tower increased the vertical velocity and power output, and increasing the diameter increased the power output. Dimensionless variables were used in a regression analysis to develop a predictive equation for power output. The predictive equation was tested with new simulations and was shown to be in very good agreement.

Acknowledgments

First, I would like to thank my advisor, Dr. Battaglia, for her guidance, support, and patience throughout my graduate studies and research. I came with a physics and math undergraduate degree not even knowing was CFD stood for, and she put in the time and effort to develop my critical thinking and research abilities. I would also like to thank Dr. Nain and Dr. Tian for offering their support and serving on my committee. Also, I would like to thank my friends in the CREST Lab for their support, feedback, and friendship.

I thank my parents, Mike and Rhonda, for their constant support as I came to Virginia Tech for a master's degree. To my brother and sister, Matt and Sydney, who were always available to get my mind off of school. Finally, I thank my best friend and fiancé, Kathryne, who was always willing to help me through my struggles and kept me motivated to stay on course. I could not have done it without any of these people.

Table of Contents

List of Figures

List of Tables

Nomenclature

A	Area
CFL	Courant-Friedrichs-Levy-Number
D	Diameter
E	Total Energy
F	Body Forces
G	Generation of Turbulent Kinetic Energy
Gr	Grashof Number
GCI	Grid Convergence Index
H	Height
I	Identity Matrix
$I(\vec{r}, \vec{s})$	Radiation Intensity
I_t	Turbulent Intensity
L	Characteristic Length
SL	Heat Source Length
N	Total Number of Cells
Q	Heat Transfer
Pr	Prandtl Number
Ra	Rayleigh Number
Re	Reynolds Number
S	Modulus of Mean Strain Rate Tensor
S_ε, S_h, S_k	Source Terms
T	Temperature
U	Maximum Fluid Velocity
W	Power
a	Absorption Coefficient
c_p	Specific Heat
$\vec{g}$	Gravity Vector
h	Enthalpy

k	Turbulent Kinetic Energy
k_{eff}	Total Conductivity
m	mass
n	Refractive Index
p	Pressure
$q"$	Heat Flux
r	Position along the Cylindrical r-axis
t	Time
u	Velocity in the x and r Direction
v	Velocity in the y Direction
$\vec{v}$	Velocity Vector
x	Position along Cartesian x-axis
y	Position along Cartesian and Cylindrical y-axis

Greek Letters

α	Thermal Diffusivity
β	Thermal Expansion Coefficient
ε	Rate of Dissipation
η	Efficiency
μ	Dynamic Viscosity
μ_t	Turbulent Viscosity
ν	Kinematic Viscosity
ρ	Density
σ	Stefan-Boltzmann Constant
σ_s	Scattering Coefficient
$\sigma_k, \sigma_\varepsilon$	Turbulent Prandtl Numbers
$\bar{\bar{\tau}}$	Stress Tensor

Subscripts

$\boldsymbol{0}$	Reference Value
$\boldsymbol{C}$	Cold
$\boldsymbol{F}$	Film
$\boldsymbol{G}$	Ground
$\boldsymbol{H}$	Hot
$\boldsymbol{S}$	Solar
$\boldsymbol{b}$	Due to Buoyancy
$\boldsymbol{k}$	Due to Velocity Gradient
$\boldsymbol{nt}$	Without a Turbine
$\boldsymbol{o}$	Outlet
$\boldsymbol{t}$	Turbine
∞	Ambient

Chapter 1. Introduction

1.1. The Solar Chimney

The most potent, dependable, and sustainable source of energy in our solar system is the sun, for which there is great interest with harnessing its power both efficiently and economically. An innovative system that is receiving more and more attention is the solar updraft tower, or solar chimney. Many researchers throughout time have explored using the updraft of heated air to generate power. Leonardo Da Vinci famously created many sketches in the early 1500s, and one of his sketched contraptions, the "smoke jack", used smoke and warm air created from a fire to power a turbine that would then spin the meat as it cooked [1]. Though the device does not use solar radiation, Da Vinci used the idea that warm air rises, which is the primary principal for the solar chimney.

In 1903, the Spanish engineer, Isodoro Cabanyes, first proposed using a solar chimney to produce electricity in his article entitled, "Projecto de motor solar" [1]. Then in 1926, Bernard Dubos, a French engineer, proposed the creation of a Solar Aero-Electric Power Plant in North Africa. His plan was to construct the power plant along the slope of the Atlas Mountains, which he claimed would increase the ascending air speed to as high as 50 m/s [1].

Finally in 1982, a team led by German civil engineer, Jörg Sclaich, constructed a solar chimney prototype in Manzanares, Spain that consisted of a 195 m high tower and a collector about 244 m in diameter [2]. The plant operated with a peak output of 50 kW, but further research determined that the efficiency of the plant improves as the overall size increases [1]. The data collected from this particular prototype proved that solar upwind power plants are a feasible source of electricity, but are highly dependent upon environmental conditions such as the requirement of sunlight and a large amount of land.

In 2001, the company, EnviroMission, began development on building the world's first large-scale solar chimney. The company's plan is to build a 200 MW plant with tower over 800 m tall with a collector diameter of 5 km [3]. In addition to being able to power around 100,000 households, this plant would have an annual savings of more than 900,000 tonnes of greenhouse CO_2 gas emissions [3]. EnviroMission choose to place thirty-two 6.25 MW turbines below the chimney capturing the horizontal air flow as it is drawn inward where the Spanish chimney had one 50 MW turbine at the base of the tower. The incredible size and achievement of the structure would capture worldwide attention and create a popular tourist attraction as well. The massive construction cost and governmental regulations are currently creating hurdles for the company, but they hope to break ground soon.

The working properties of the solar chimney rely on the buoyant nature of air to turn a turbine that generates electricity. The system consists of three primary pieces: the chimney, collector, and turbine. The chimney is a large pressure tower that is typically made from adiabatic materials such as cement. The collector is made of transparent material such as glass or polycarbonate and functions similarly to that of a greenhouse. The turbine operates as a shrouded pressure-staged wind generator, which converts pressure into energy using cased turbines [4]. There is a pressure drop across the turbine, but the velocity before and after remains about the same. The schematic for the solar chimney power plant is shown in Figure 1.1. Part (a) shows the path that the air moves within the plant, while part (b) depicts the heating of the air below the collector during the day and night. Beginning with part (a), solar radiation passes through the collector surface and warms the air below, which causes the air to rise. As the air flows up and out of the chimney, new air is drawn inward from the perimeter towards the chimney where the process repeats. The turbine is located towards the lower section of the chimney and converts the traveling air into electricity

that is then sent to a generator. Next with part (b), during the day, solar radiation passes through the collector where the rays either strike the air molecules or the ground. The rays that strike the air molecules heat the air, while the ones that strike the ground are either absorbed or reflected back to the collector, which are reflected creating a continuous process. Eventually, both the air and ground are heated. Due to the ground being porous, the stored energy can continue to warm the air throughout the night. The amount of energy released from the ground can be increased with underground thermal storage systems that absorb and hold more radiation from the sun [2].

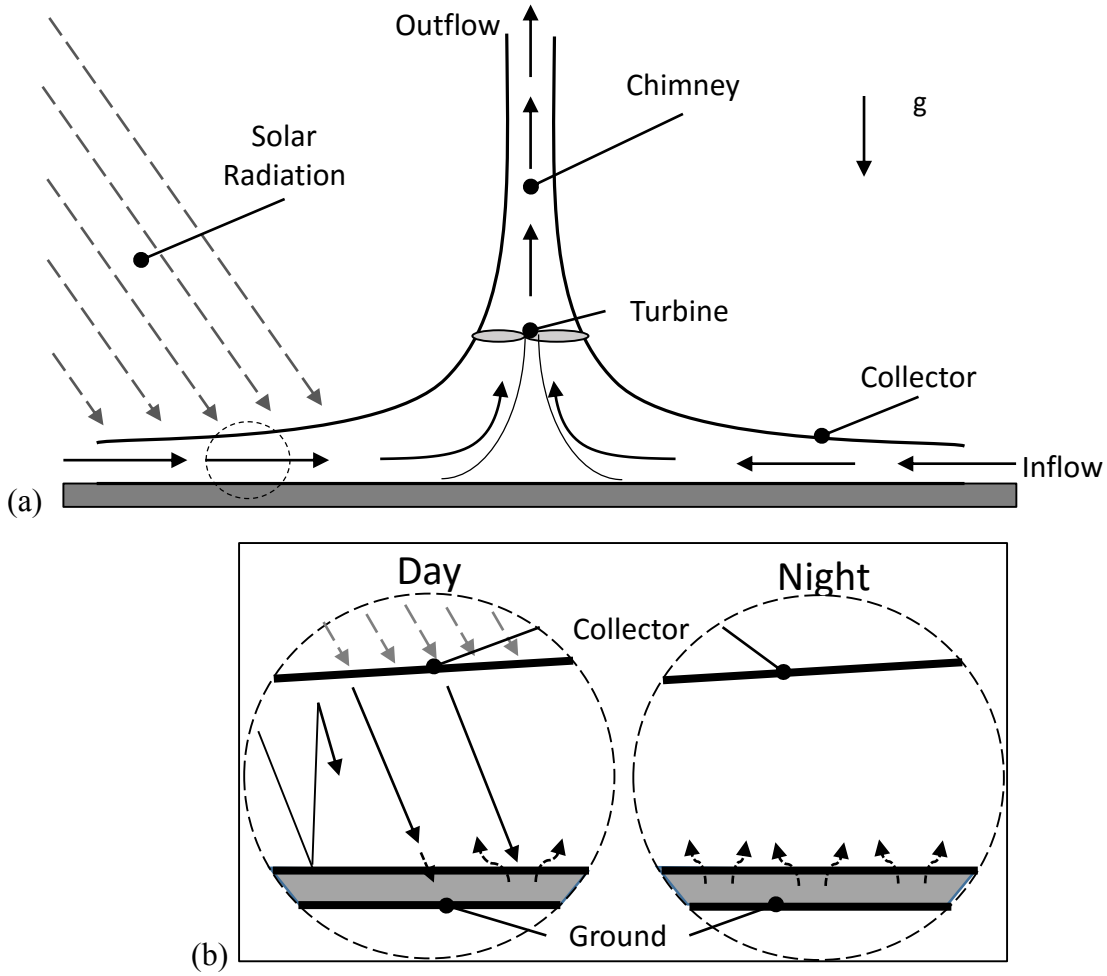

Figure 1.1: (a) Schematic of solar chimney power plant system and (b) enlarged region in the collector to highlight energy transfer during day and night

The size of the collector and tower both directly impact the cost and efficiency of the power plant. As the size is increased, the cost and efficiency do as well. Increasing the diameter of the collector increases the heat transfer within the system, which increases the air velocity. Increasing the temperature difference between the ambient and measured within the tower increases the pressure difference, and therefore, the air velocity as well. Due to the size of a solar chimney, many acres are necessary for instalment, but the system can also function as a greenhouse so that the vegetation below the collector can thrive [5]. Overall, the solar upwind power plant is a viable source of solar energy due to its low maintenance costs and positive impact on vegetation, but it is situational due to its solar radiation requirements, massive upfront construction cost, and large overall size.

1.2. Motivation

Two major problems, poverty and worldwide dependence on fossil fuels, are prevalent in society. Fossil fuels are nonrenewable source of pollution, and poverty negatively affects the livelihood of millions worldwide. There is a severe need to reduce fossil fuel emissions, but with the ever growing demand for energy, how could limiting consumption of fossil fuels be possible without having severe economic impacts? The answer is teaming both fossil fuels and renewable clean energy where it makes sense economically, socially, and geographically. In addition, the livelihoods of impoverished people can be dramatically improved with cheap energy. Energy can improve the sanitation of food and water, make many educational tools possible, allow students to study during the night, bolster the local economy by setting up an encouraging location for businesses, and much more. Using renewable energy sources such as the solar upwind power plant, humanity can move towards improving both of these problems.

Rural Africa would greatly benefit from a solar upwind power plant. Many villages are without sufficient electricity, such that the children are forced to perform school work with candles and below street lights. In 2013, with 70% of the population in Sub-Saharan Africa without electricity, the Obama administration announced the "Power Africa" initiative, which established global goals to increase the access to reliable power for more people in Sub-Saharan Africa by using primarily "green solutions" [6]. Overall, this location is a perfect spot for a solar chimney power plant due to the abundance of solar radiation. The continent of Africa has the highest solar irradiation and receives between 6 to 7 $kW \cdot h/m^2$ daily horizontal (total) irradiation [7]. Total irradiation is the sum of the direct normal irradiance and diffuse horizontal irradiance. A majority of Africa receives much more solar radiation than Manzanares, Spain, where a successful prototype has already been implemented. Smaller towers are possible in locations where solar radiation is more significant due to increasing temperatures below the collector [8]. Africa is an ideal location for the solar updraft power plant to meet the goal to bring clean energy to this remote area.

A solar chimney would be a great fit for rural Sub-Saharan Africa. With plenty of land, this technology would be able to provide clean and renewable energy both day and night to an entire village. During construction, many people would be provided quality jobs, and after construction, the new electricity would bolster the local economy with the new ability to drastically improve local education and provide a business friendly environment. Improving the living conditions of the impoverished people in rural Africa is a goal that can be achieved by supplying reliable access to electricity. Due to the geographic locations, exposure to the sun, and the low maintenance costs, the solar chimney could provide clean renewable energy in Sub-Saharan Africa if the initial construction cost could be solved.

1.3. Recent Work in Computational Fluid Dynamics

After the success of the prototype in Manzanares, Spain, there are more and more solar chimney prototypes and proposals. With the substantial construction cost, further research is required to fully understand the functionality of the solar updraft technology. Computational fluid dynamics (CFD) is a numerical tool that evaluates the system using cheaper and quicker methods compared to the construction of physical prototypes. With many commercial codes available, determining the proper code and methods are imperative to fully understanding the system. Since the early 2000s, many researchers have modeled solar chimneys and are still making dramatic strides.

In 2004, nearly 20 years after the construction of the prototype in Spain, Pastohr et al. [9] conducted a CFD study of the Manzanares tower with the goal of analyzing the thermal storage system. In their study, Fluent was used to create an axisymmetric solar chimney model using the parameters from the Spanish power plant and included two meters of ground thermal storage. Instead of including a radiation model, the authors decided to use a thin layer above the ground that acted as a heat source [9]. With their model, the authors were able to determine profiles for the temperature, velocity, and pressure. They concluded that increasing the amount of energy put into the system increased the velocity of the air moving within the system. In addition, Pastohr et al. [9] developed mathematical models based on an energy balance between the ground and collector. Finally comparing the two models, the authors concluded that a transient simulation is needed to accurately calculate the heat transfer between the ground and collector Later in 2010, Xu et al. [10] developed an axisymmetric model of a solar chimney nearly identical to that of Pastohr et al. [9] but with a different thermal storage model. Xu et al. [10] used a porous material, whereas Pastohr et al. [9] modeled the thermal storage system as a solid material. In addition, Xu

et al. [10] also added a model for the turbine by using a pressure drop at the junction between the collector and chimney. The theoretical turbine efficiency and power output were used to determine the proper pressure drop. With this model, Xu et al. [10] determined that the power output and energy lost from the turbine are directly related to the amount of solar radiation and the turbine efficiency.

In 2008, a study modeling the thermal storage layers with porous materials was performed by Ming et al. [11]. While a solid material only considers conduction heat transfer, a porous material considers conduction along with both convective and radiative transfer as well. This study concluded that using materials with a higher thermal conductivity resulted in a higher daily amount of heat stored, and therefore, are better suited for the thermal storage layer [11]. In addition, the solar radiation impact on pressure, velocity, and temperatures were studied as well. As the solar radiation increased, the velocity and temperature increased and the pressure decreased [11]. Overall, this study provided insight on optimizing the thermal storage system as well as the effects of the solar radiation on the system.

The size of the chimney and its impacts on the turbine efficiency was studied by Fasel et al. [12] in 2013. They created different scaled models to test the impact caused by different sized towers. The authors scaled each model from the prototype in Manzanares, Spain and held the boundary conditions and solution methods constant. Increasing the overall size of the solar chimney resulted in an increase of both the temperature and velocity inside the system.

With the heat transfer in the solar chimney being due to natural convection, many researchers have performed CFD studies to better understand this process. In 2010, Chergui et al. [13] created a model with no turbine or thermal storage system to isolate and observe the air movement within the system. The air flow was controlled by the boundary conditions. After a temperature

difference was calculated using the Rayleigh number equation, the lower temperature was set to the chimney walls and the higher temperature was set to the ground. The difference affected the flow dramatically. As the Rayleigh number was increased, the flow within the system transitioned from laminar to turbulent flow. Chergui et al. [13] concluded that the turbulence was fully developed with a Rayleigh number of 10^8 while a Rayleigh number of 10^6 predicted laminar flow. This was not the only study observing the effect of the Rayleigh number effect. In 2012, Tahar et al. [14] expanded on the study of Chergui et al. [13] by altering the shape of the chimney by using a curved junction. Tahar et al. [14] reached a similar conclusion except that the turbulence began with a Rayleigh number as low as 10^5. Overall, the two studies provided further insight for the airflow within the system and concluded that increasing the Rayleigh number eventually led to a change from laminar to turbulent flow.

Due to the extensive size of the solar updraft tower, computational fluid dynamics is a great tool as it offers a much cheaper and accessible format of research compared to physically building new prototypes. The previous studies have all brought more insight in the modeling of solar chimneys such as using a radiation model to accurately calculate the heat loss, a transient model with a thermal storage layer to accurately calculate the heat transfer from the ground to the air, and a porous medium to accurately model the thermal storage system. Even with different models, many of the studies came to similar conclusions such as increasing solar radiation increases the temperature and velocity and using a pressure drop to represent the turbine increased the efficiency of the system. Overall, these studies have provided more understanding to the impacts of the individual sections and processes on the solar chimney system. Even with these advances, researchers are still striving for a more accurate CFD model.

1.4. Objectives

The objective of this thesis is to develop a simplified numerical model for the solar chimney power plant to investigate the effects of the geometry and turbine location on the flow and power output. Decreasing the overall tower height would decrease the overall construction cost and improve the appearance of the chimney but also decrease the power output and efficiency of the system. A goal of this thesis is to further investigate the geometry effects on the output of the system. The numerical model will be simplified by employing a two-dimensional domain that does not include a layer to represent the thermal storage of the ground or a solar radiation model. Also using a simplified model for the turbine will allow the generated power output to be calculated without physically modeling the turbine load. Further knowledge on solar chimneys and the flow within would be beneficial to eventually implementing one in Sub-Saharan Africa because there is a large amount of cheap available land. The thesis will use both analytical and numerical models to accomplish the goal of understanding the amount of power generated. Both the numerical and analytical models will be compared and validated with experimental data extracted from the solar chimney built in Manzanares, Spain [15]. In addition, a statistical prediction equation will be created from the numerical data to predict the power output from the outlet velocity and outlet temperature.

1.5. Organization of the Thesis

Chapter 2 presents the numerical methods and assumptions to solve the Navier-Stokes equations required for this study. The governing equations, turbulence modeling, and discretization methods are discussed along with their specific simplifications. In addition, a dimensionless variable study is also shown in Chapter 2 to ascertain the characteristic length scale. To be confident in the accuracy of the methodology and modeling, three validation cases are

performed and presented in Chapter 3. The different studies investigate the airflow of a free plume, the Rayleigh number effects of the air within a solar chimney, and the proper methods of modeling the turbine and energy storage layer. First, the work of Schaelin et al. [16] for the free plume case provides background knowledge in convection by using a one-dimensional line to model a heat flux. The free plume case is also used to explore different solvers, turbulence models, and discretization procedures. The studies of Chergui et al. [13] and Tahar et al. [17] are then used to investigate the definition of the Rayleigh number and its effect on the flow within the solar chimney in addition to properly modeling with an axisymmetric domain. Lastly, the work by Xu et al. [10] provides insight on modeling the heat source of the ground, the pressure drop of the turbine, and using a convection coefficient to model the collector boundary condition. Chapter 4 develops a numerical model of a solar chimney and compares it to the experimental data and an analytical model. The resulting airflow from the numerical model is investigated including the effects from the turbine pressure drop. Chapter 5 presents the conclusion of the thesis and provides recommendations for future work.

Chapter 2. Numerical Approach

2.1. Governing Equations

The commercial code ANSYS Fluent [18] is used for the simulations in this work. The fundamental governing equations are summarized and important assumptions are explained. The equation for conservation of mass, or continuity, is:

$$\frac{\partial \rho}{\partial t} + \nabla \cdot (\rho \vec{v}) = 0 \quad (1)$$

where t is time, ρ is density, and $\vec{v}$ is the velocity vector. Next, the conservation of momentum is:

$$\frac{\partial}{\partial t}(\rho \vec{v}) + \nabla \cdot (\rho \vec{v} \vec{v}) = -\nabla \mathrm{p} + \nabla \cdot (\bar{\bar{\tau}}) + \rho \vec{g} \quad (2)$$

where p is the static pressure, $\vec{g}$ is the gravitational vector, and $\bar{\bar{\tau}}$ is the stress tensor, which is expressed as:

$$\bar{\bar{\tau}} = \mu \left[(\nabla \vec{v} + \nabla \vec{v}^T) - \frac{2}{3} \nabla \cdot \vec{v} I \right] \quad (3)$$

where I is the identity tensor, μ is the dynamic viscosity. Finally, the conservation of energy equation is:

$$\frac{\partial}{\partial t}(\rho E) + \nabla \cdot \left(\vec{v} (\rho E + p) \right) = \nabla \cdot k_{eff} \nabla \mathrm{T} + \nabla \cdot (\bar{\bar{\tau}} \cdot \vec{v}) + S_h \quad (4)$$

where S_h is an energy source term and E is the total energy within the system, which contains the potential, kinetic, and internal energy. The total conductivity, k_{eff}, combines both the thermal conductivity of the fluid and the turbulent thermal conductivity. The enthalpy of the fluid or internal energy, h, is expressed:

$$h = \int_{T_0}^{T} c_p \, dT \quad (5)$$

where c_p is the constant pressure specific heat. There are many assumptions that will simplify these governing equations, as discussed next.

The Boussinesq model can be assumed for the buoyancy force in the momentum equation where the temperature is assumed to be a function of density. This assumption can only be implemented with small temperature differences. By defining the thermal expansion coefficient, β, as:

$$\beta = -\frac{1}{\rho}\left(\frac{\partial \rho}{\partial T}\right)_p \approx -\frac{1}{\rho}\frac{\rho_0 - \rho}{T_0 - T} \quad (6)$$

and assuming small temperature changes in the chimney system, the density can be expressed as:

$$(\rho - \rho_0) \approx -\rho_0 \beta (T - T_0) \quad (7)$$

where the subscript *0* represents the reference value. Equation (7) calculates the density from the reference density. The reference density is constant and substituted into the conservation of mass and energy equations (Equations (1) and (4)). For the conservation of momentum equation (Equation (2)), the density in the left-hand side is expressed by the reference density and the density in the right-hand side is expressed as the density calculated from Equation (7). If the fluid is assumed to be incompressible, the continuity equation can be simplified to:

$$\nabla \cdot \vec{v} = 0 \quad (8)$$

Also, assuming a Newtonian fluid, the stress tensor, Equation (3), can be simplified:

$$\bar{\bar{\tau}} = \mu \nabla \vec{v} \quad (9)$$

Substituting Equation (9) into the momentum equation (Equation (2)) results in a simplified energy equation because the viscous heating term, $\nabla \cdot (\bar{\bar{\tau}} \cdot \vec{v})$, can be neglected. In addition, the

energy source term can be neglected. With all of these assumptions, the momentum and energy equations can be simplified to:

$$\frac{\partial \vec{v}}{\partial t} + \vec{v}\,\nabla \cdot \vec{v} = -\frac{1}{\rho_0}\,\nabla \rho + \frac{\mu}{\rho_0}\,\nabla^2 \vec{v} + \vec{g}\,[1 - \beta(T - T_0)] \qquad (10)$$

$$\frac{\partial T}{\partial t} + \vec{v} \cdot \nabla T = \alpha \nabla^2 T \qquad (11)$$

where $\alpha = k/(\rho\, c_p)$.

2.2. Turbulence Modeling

Both the standard and realizable $k - \varepsilon$ turbulence model are used throughout this study, and both assume that the flow is fully turbulent so that the effects of molecular viscosity can be neglected. For the standard $k - \varepsilon$ turbulence model, the turbulence kinetic energy, k, and its rate of dissipation, ε, are calculated from the transport equations [18]:

$$\frac{\partial}{\partial t}(\rho k) + \nabla \cdot (\rho k \vec{v}) = \nabla \cdot \left[\left(\mu + \frac{\mu_t}{\sigma_k}\right)\vec{k}\right] + G_k + G_b - \rho\varepsilon \qquad (12)$$

$$\frac{\partial}{\partial t}(\rho \epsilon) + \nabla \cdot (\rho \epsilon \vec{v}) = \nabla \cdot \left[\left(\mu + \frac{\mu_t}{\sigma_\epsilon}\right)\vec{\epsilon}\right] + C_{1\epsilon}\,\frac{\epsilon}{k}\,(G_k + C_{3\epsilon} G_b) - C_{2\epsilon}\,\rho\,\frac{\epsilon^2}{k} \qquad (13)$$

where σ_k and σ_ε are the turbulent Prandtl numbers for k and ε, and $C_{1\varepsilon}$, $C_{2\varepsilon}$, and $C_{3\varepsilon}$ are constants. The generation of turbulence kinetic energy due to the mean velocity gradients, G_k, is expressed:

$$G_k = \mu_t\, S^2 \qquad (14)$$

where S is the modulus of the mean rate-of-strain tensor and defined as:

$$S \equiv \sqrt{2\, S_{ij} S_{ij}} \qquad (15)$$

The generation of turbulence kinetic energy due to buoyancy, G_b, is expressed:

$$G_b = -\vec{g}\beta\frac{\mu_t}{\rho\, Pr}\nabla T \quad (16)$$

The turbulent viscosity, μ_t, is defined as:

$$\mu_t = \rho\, C_\mu \frac{k^2}{\epsilon} \quad (17)$$

where C_μ is based on the mean rate of strain and rotation, the angular velocity, and the system rotation. The parameters in Equations (12) and (13) are defined as $C_{1\varepsilon} = 1.44$, $C_{2\varepsilon} = 1.92$, $\sigma_k = 1.0$, and $\sigma_\varepsilon = 1.3$ [18]. The third constant, $C_{3\varepsilon}$, is not specified, but calculated using a relationship between the velocity vector parallel and perpendicular to the gravitational vector:

$$C_{3\epsilon} = \tanh\left|\frac{v}{u}\right| \quad (18)$$

For the realizable $k - \varepsilon$ turbulence model, the turbulence kinetic energy and rate of dissipation are calculated using the transport equations [18]:

$$\frac{\partial}{\partial t}(\rho k) + \nabla\cdot(\rho k\vec{v}) = \nabla\cdot\left[\left(\mu + \frac{\mu_t}{\sigma_k}\right)\vec{k}\right] + G_k + G_b - \rho\varepsilon \quad (19)$$

$$\frac{\partial}{\partial t}(\rho\epsilon) + \nabla\cdot(\rho\epsilon\vec{v}) = \nabla\cdot\left[\left(\mu + \frac{\mu_t}{\sigma_\epsilon}\right)\vec{\epsilon}\right] + \rho C_1 S_\varepsilon - \rho C_2\frac{\epsilon^2}{k+\sqrt{v\epsilon}} + C_{1\epsilon}\frac{\epsilon}{k}C_{3\epsilon}G_b \quad (20)$$

There are many overlap between the two models so G_k is defined in Equation (14), G_b is defined in Equation (16), μ_t is defined in Equation (17), and $C_{3\varepsilon}$ is defined in Equation (18). Similarly to before, ANSYS Fluent defines the parameters as $C_{1\varepsilon} = 1.44$, $C_2 = 1.9$, $\sigma_k = 1.0$, and $\sigma_\varepsilon = 1.3$. The new variable, C_1, is expressed:

$$C_1 = max\left[0.43, \frac{S\frac{k}{\epsilon}}{S\frac{k}{\epsilon}+5}\right] \quad (21)$$

The two different turbulence models will be compared throughout the following studies.

2.3. Grid Resolution Study

A grid resolutions study is necessary to decrease the amount of numerical error resulting from the mesh. The grid convergence index (GCI) method used to define the numerical error and create an extrapolated profile was discussed by Celik et al. [19] and is summarized here. The first step is to define the representative cell:

$$h = \left(\frac{1}{N}\sum_{i=1}^{N} A_i\right)^{1/2} \quad (22)$$

where N is the total number of cells within the mesh and A_i is the area of the *i*th cell. For this particular study, three different grid resolutions are necessary such that the refinement factor between the finest and coarsest mesh, $r = h_{coarse}/h_{fine}$, must be greater than 1.3. Let the subscripts 1, 2, and 3 represent the fine, medium, and coarse mesh, respectively, such that $h_1 < h_2 < h_3$. Next, the apparent order, *p*, is calculated:

$$p = \frac{1}{ln(r_{21})}\left|ln\left|\frac{\varepsilon_{32}}{\varepsilon_{21}}\right| + q\right| \quad (23)$$

$$q = ln\left|\frac{{r_{21}}^p - s}{{r_{32}}^p - s}\right| \quad (24)$$

$$s = 1 * sgn\left(\frac{\varepsilon_{32}}{\varepsilon_{21}}\right) \quad (25)$$

where $r_{21} = h_2/h_1$, $r_{32} = h_3/h_2$, $\varepsilon_{21} = \phi_2 - \phi_1$, and $\varepsilon_{32} = \phi_3 - \phi_2$ such that ϕ_k represents a particular variable of the *k*th mesh. Equation (24) is first solved with a dummy *p* value, and then substituted into Equation (23). Then through iteration, the proper apparent order is obtained. Next, the extrapolated values are calculated:

$$\phi_{ext}^{21} = \frac{{r_{21}}^{p}\,\phi_1 - \phi_2}{{r_{21}}^{p} - 1} \quad (26)$$

The extrapolated values will be used to compare property profiles of numerical validations. In addition, the error estimates with the apparent order of p are defined:

$$e_a^{21} = \left|\frac{\phi_1 - \phi_2}{\phi_1}\right| \quad (27)$$

$$e_{ext}^{21} = \left|\frac{\phi_{ext}^{21} - \phi_1}{\phi_{ext}^{21}}\right| \quad (28)$$

$$GCI_{fine}^{21} = \frac{1.25\, e_a^{21}}{{r_{21}}^{p} - 1} \quad (29)$$

where e_a^{21} is the approximate relative error, e_{ext}^{21} is the extrapolated relative error, and GCI_{fine}^{21} is the fine grid convergence index. Each validation case will present a grid resolutions study, calculating the apparent order and fine-grid convergence index at multiple locations, and also presenting property profiles with the calculated extrapolated values.

2.4. Discretization Methods

The governing equations are solved using a pressure-based solver with a finite volume discretization. The geometry and mesh are created in ICEM and imported into Fluent where the cells are control volumes used to solve the fluid properties. With the pressure-based solver for incompressible flow, pressure becomes the primitive variable. The semi-implicit method for pressure linked equations (SIMPLE) algorithm is chosen to couple the pressure and velocity equations [18]. The SIMPLE algorithm uses the momentum equation to estimate a pressure and then corrects both the pressure and velocity until the conservation of mass equation is satisfied. The resulting velocity and pressure are calculated:

$$\vec{v} = \vec{v}^{*} - \vec{v}' \quad (30)$$

$$\vec{p} = \vec{p}^{*} - \vec{p}' \quad (31)$$

where $\vec{v}'$ is the velocity correction and $\vec{p}'$ is the pressure correction. The relationship to couple the variables is:

$$\vec{v}' = -\frac{1}{A_P}\sum_{l} A_l \, \vec{v}'_l - \frac{1}{A_P}\nabla \cdot p'|_p \quad (32)$$

where A_P and A_l are coefficients from the discretized momentum equations. The subscripts P and l represent an individual velocity node and the neighbor points that appear in the discretized conservation of momentum equation. Substituting the corrected velocity equation into the discretized continuity equation results in the pressure-correction equation:

$$\nabla \cdot \left[\frac{\rho}{A_P} \nabla \cdot \rho'\right]_P = [\nabla \cdot (\rho \vec{v}^{*})]_P + [\nabla \cdot (\rho \vec{v}')]_P \quad (33)$$

Beginning with Equation (33) the second term is not known so it is neglected. The resulting pressure correction is then substituted into Equation (32) to calculate the velocity correction, which is substituted into Equation (33). This is iterated until the continuity equation is solved.

The second-order upwind interpolation, based on a Taylor-Series expansion about the center of a cell using the values of two cells upwind, is implemented to discretize the momentum, energy, radiation, and turbulence equations. The pressure discretization employs pressure staggering (PRESTO!) scheme. The least squares cell based method is used for the gradient and spatial discretization. For transient simulations, time is discretized using a first-order implicit method where a Courant-Friedrichs-Levy (CFL) number of 1 is used to determine the time step size. CFL is defined:

$$CFL = \frac{U \, \Delta t}{\Delta x} \quad (34)$$

where U is the maximum fluid velocity, Δx is the smallest cell size, and Δt is the time step size. An absolute convergence criteria of 10^{-8} is used throughout unless indicated otherwise.

2.5. Rayleigh Number

To define the Rayleigh number, dimensionless variables are created using the variables: u_0, ρ_0, L. The dimensionless variables are represented with the superscript * and are simplified to:

$$t^* = t\,\frac{u_0}{L} \tag{35}$$

$$\nabla^* = \nabla L \tag{36}$$

$$\vec{v}^* = \frac{\vec{v}}{u_0} \tag{37}$$

$$g^* = g\,\frac{L}{{u_0}^2} \tag{38}$$

$$p^* = \frac{p}{\rho_0\,{u_0}^2} \tag{39}$$

$$T^* = \frac{T - T_\infty}{T_H - T_\infty} \tag{40}$$

Substituting these dimensionless variables into governing equations, Equations (1), (10), and (11), results in:

$$\nabla^* \cdot \vec{v}^* = 0 \tag{41}$$

$$\frac{\partial\,\vec{v}^*}{\partial\,t^*} + \vec{v}^*\nabla^* \cdot \vec{v}^* = -\nabla^* p^* + \frac{1}{Re}\nabla^{*2}\,\vec{v}^* - \frac{Gr}{Re^2}\,T^* + g^* \tag{42}$$

$$\frac{\partial\,T^*}{\partial\,t^*} + \vec{v}^* \cdot \nabla^* T^* = \frac{1}{Pr\,Re}\nabla^{*2} T^* \tag{43}$$

where Re is the Reynolds number, Gr is the Grashof number, and Pr is the Prandtl number and are represented as:

$$Re = \frac{\rho_0 u_0 \, L}{\mu} \quad (44)$$

$$Gr = \frac{\vec{g}\beta \, (T_H - T_\infty) L^3}{\nu^2} \quad (45)$$

$$Pr = \frac{\nu}{\alpha} \quad (46)$$

The Reynolds number is the ratio of momentum forces to viscous forces, the Grashof number is the ratio of buoyancy forces to viscous forces, and the Prandtl number is the dimensionless energy equation. In addition, the Rayleigh number will be investigated and is the product of the Grashof and Prandtl numbers:

$$Ra = \frac{\vec{g}\beta \, (T_H - T_\infty) L^3}{\nu \, \alpha} \quad (47)$$

In the following chapters, the simplified conservation of mass, momentum, and energy equations will be solved to investigate the solar chimney power plant. In addition, the SIMPLE and PRESTO! schemes will be employed to discretize and properly model the pressure. Finally, the turbulence models are necessary as the air within the system is turbulent, and both the realizable and standard k-ε turbulence models will be investigated.

Chapter 3. Validation Cases

3.1. Free Plume

In 1992, Schaelin et al. [16] modeled a two-dimensional free plume in ambient conditions using a one-dimensional heat source in a Cartesian coordinate system. The ambient air temperature was 293 K and the heat source was 100 W/m. The schematic for the system is shown in Figure 3.1. The domain is 61 m wide by 100 m tall where both the top and sides are defined by ambient conditions, the bottom is the ground, and the heat source is at the midpoint of the ground defined with a constant heat flux. Schaelin et al. [16] used a coarse non-uniform mesh of 45 by 34 cells where the finest cell was at the center of the bottom face near the heat source [16]. The authors also wrote their own code to run this case.

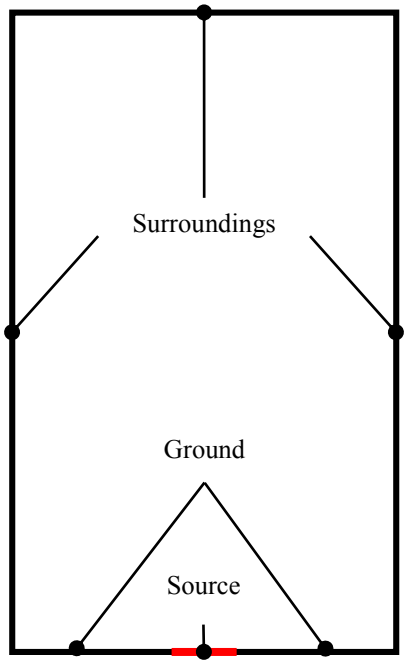

Figure 3.1: Schematic of free plume in ambient conditions

For the validation study, a geometry similar to Schaelin et al. [16] is used, and a source length (shown in red in Figure 3.1) of 0.2 m is assumed because Schaelin et al. [16] did not provide the dimensions. The ground is modeled as an adiabatic no-slip wall, the top and sides are modeled with the ambient temperature (T_∞ = 293 K) and pressure (1 atm), no turbulent backflow, and the heat source is modeled as a no-slip wall with a heat transfer per unit width of 100 W/m^3. Due to the improvements of computers since 1992, a much finer mesh can be used to discretize the domain. The non-uniform 160 by 100 cell mesh is presented in Figure 3.2. The air properties are defined at ambient conditions and the flow is assumed steady-state. The finest cells are 0.02 m by 0.1 m, which is located directly above the heat source. The flow effects using different solver types, turbulence models, and discretization orders are compared by observing property contours and vertical velocity profiles along the centerline.

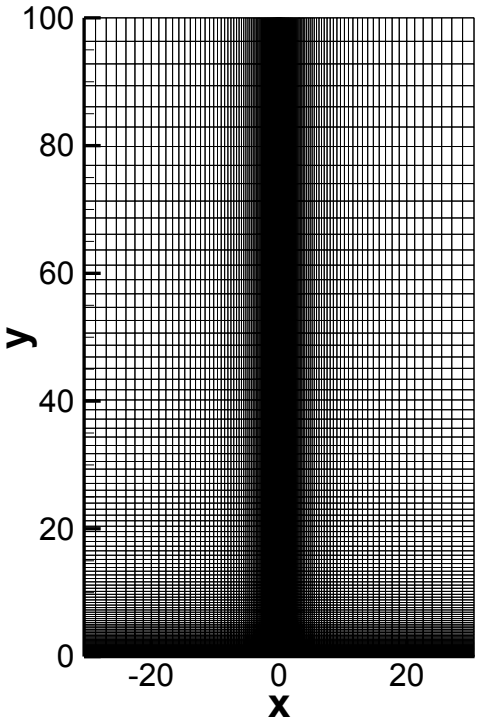

Figure 3.2: Generated mesh for free plume study

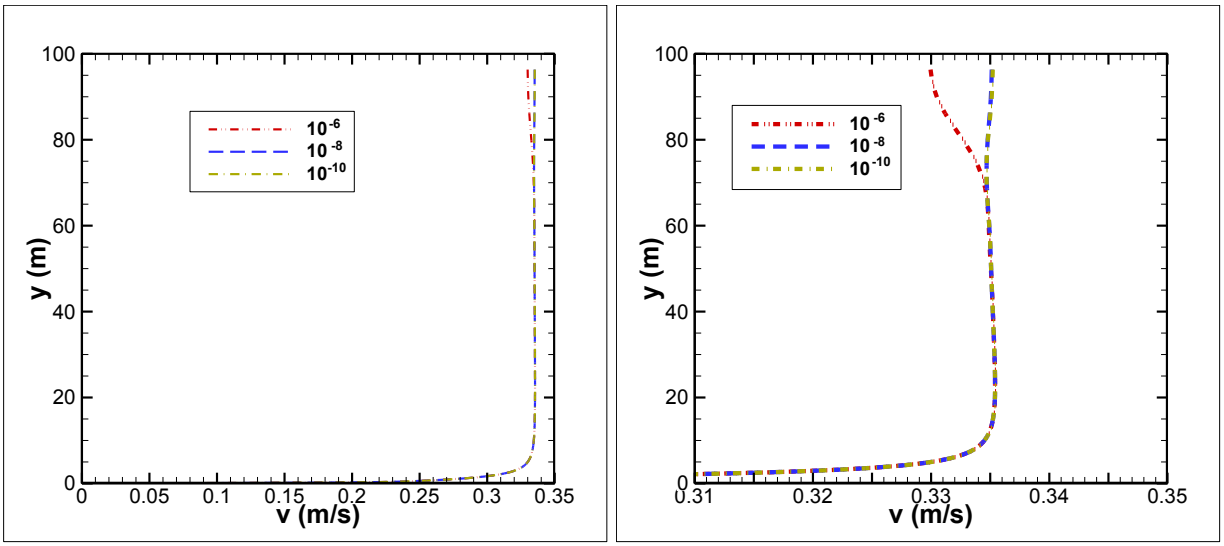

Figure 3.3: Convergence study for pressure-based solver, realizable k-ε turbulence model, and second-order upwind discretization; vertical position versus vertical velocity along the centerline

A convergence case study is performed to find the proper residual criteria that indicate the flow has reached steady-state. For the convergence study, the pressure-based solver, realizable k-ε turbulence model, and second-order spatial discretization are used and the corresponding vertical velocities along the centerline are shown in Figure 3.3. Both plots represent the same values, but the right plot is magnified by reducing the scale along the *v*-axis so that the discrepancies are more visible. When the residuals are 10^{-6}, the vertical velocity begins to decrease at a height of about 65 m, and when the residuals reach 10^{-8} or higher, the velocity is constant after it reaches its peak value. The study concludes that the solution reaches steady-state when the residuals reach 10^{-8} and therefore, this criteria are used for the simulation going forward.

Different solvers, turbulence models, and discretization solvers are tested and compared; pressure-based and density-based solvers, standard *k-ε* and realizable *k-ε* turbulence models, and the first-order and second-order upwind discretization solvers. The vertical velocities along the centerline for the different cases are presented in Figure 3.4. The base case will be defined with

the pressure-based solver, realizable k-ε turbulence model, and second-order upwind discretization, which is present on each plot to compare the effects of the chosen numerical method.

In Figure 3.4, all cases are compared in part (a), while the other three plots are magnified to better show the effects of the numerical methods on the flow. Part (b) compares the density-based method to the pressure-based, part (c) compares the realizable turbulence model to the standard model, and part (d) compares the first-order upwind to the second-order. Beginning with part (b), the density and the pressure based methods have insignificant differences, and therefore, the pressure-based solver was chosen because it reaches steady-state with fewer iterations. As shown in part (c), the turbulence models significantly affect the peak velocity. The standard turbulence model has a peak velocity of 0.320 m/s, while the realizable turbulence model has a peak velocity of 0.335 m/s. Finally for part (d), the degree order of discretization has a significant effect as well, though not as significant as the turbulence model. The first-order upwind spatial discretization results in a peak velocity of 0.339 m/s compared 0.335 m/s from the second-order upwind. Schaelin et al. [16] found that their model had a similar profile shape, a peak velocity of 0.35 m/s, and an air temperature of 21.6 ˚C one meter above the heat source [16]. The pressure-based, realizable *k-ε* turbulence model with first-order upwind discretization had the closest peak velocity and the air temperature one meter above the heat source was approximately 21.9 ˚C; therefore, this case is used going forward.

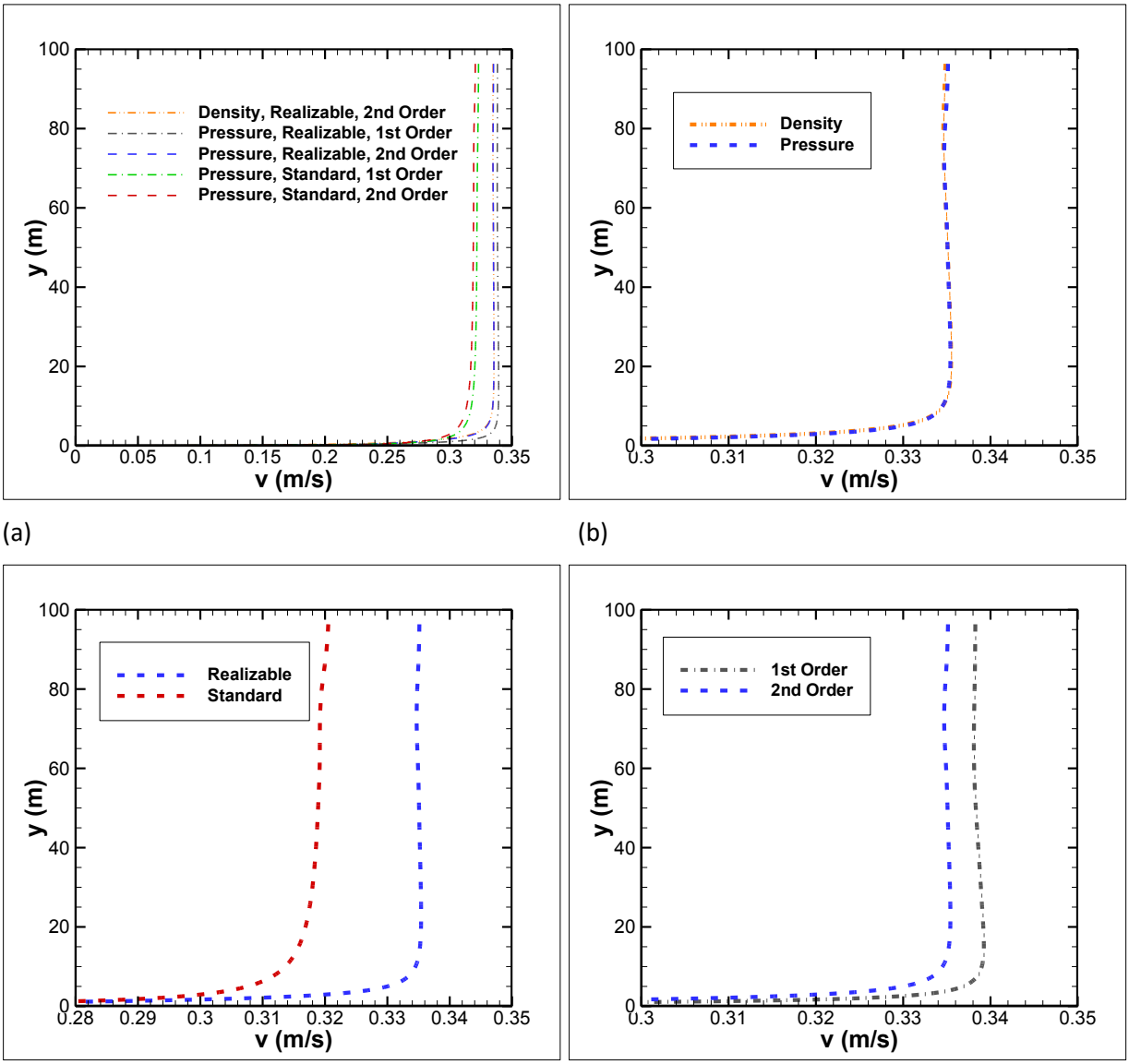

Figure 3.4: Vertical position versus vertical velocity comparing (a) all cases, (b) solvers, (c) turbulence models, and (d) discretization solvers

Schaelin et al. [16] investigated the flow properties of pressure, velocity, and turbulence intensity. The contours of the current study are presented in Figure 3.5 and provide important information on the flow of air within the system and are compared to the results shown in Schaelin et al. [16] (but not included here). Beginning with the vertical velocity, as the height increases, the width of the plume also increases. After 10 m, the height does not affect the peak velocity. Next, the turbulent intensity contours are similar to the velocity where the width increases with height, but it is noticeable that the maximum value is not in the center. Using both vertical velocity and turbulent intensity contours as references, the realizable k-ε turbulence model results in a wider plume than the standard model. The results shown in Figure 3.5a-c are consistent with the findings of Schaelin et al. [16]. Finally for the pressure, although the differences are small, the pressure is positive where the plume is present and negative everywhere else. There are also two negative regions of pressure at the top of the domain created from the boundary condition. Overall, the results found in the current study predict the same physics and features found by Schaelin et al. [16].

In conclusion, the modeling methods were validated by comparing the current study to the free plume case found in Schaelin et al. [16] . It was shown that the best models to predict fluid flow coupled with heat transfer are the pressure-based solver, realizable k-ε turbulence model, and first-order spatial discretization. Overall, the current study using ANSYS Fluent was validated and a deeper knowledge on the different computational models was acquired going forward. These particular models will be employed in the remaining studies throughout the thesis.

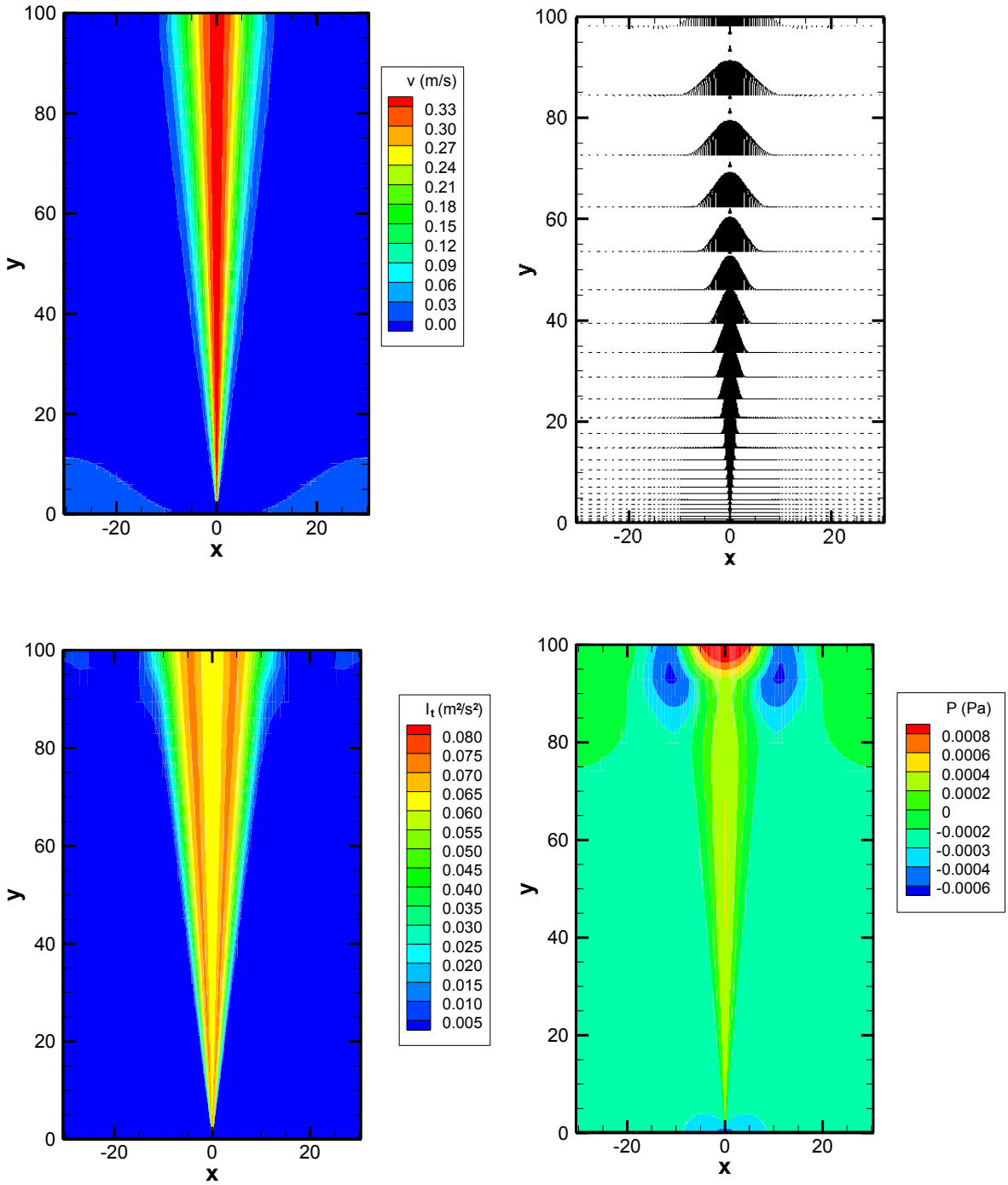

Figure 3.5: Free plume property figures; velocity vectors, turbulent intensity, and pressure

3.2. Solar Chimney

Studies that modeled a solar chimney are used to further investigate the modeling that will be employed for the solar power plant. Chergui et al. [13] and Tahar et al. [17] modeled a solar chimney to investigate the transition from laminar to turbulent flow. The basic schematics of the solar chimneys are shown in Figure 3.6 for Chergui et al. [13] and Tahar et al. [17], respectively. To simplify the computations, these authors specified temperatures at each surface to avoid using radiation models to replicate the effects of the sun. What is interesting about these studies is that the reported Rayleigh numbers for transition do not agree. Thus, as part of this validation, an in-depth analysis will be pursued to determine the proper method to define the Rayleigh number.

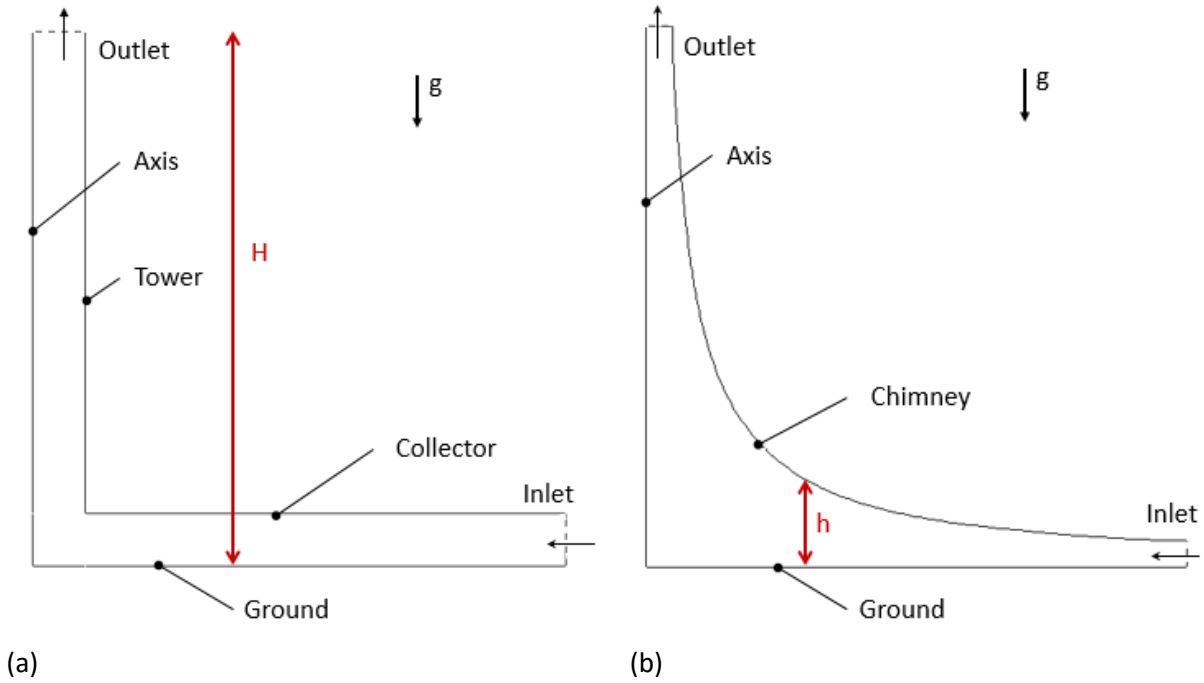

Figure 3.6: Solar chimney schematics; (a) perpendicular junction from Chergui et al. [13], (b) curved junction from Tahar et al. [14]

The Rayleigh number is used to define the flow characteristics between two plates of differing temperatures. Laminar flow is when the flow travels in parallel layers, and turbulent flow is when

the velocity varies erratically in magnitude and direction. For natural convection of a free plume, the Rayleigh number transition between laminar and turbulent flow is typically on the order of 10^9. For internal flow, there is not a clear consensus as to the critical Rayleigh number for transition. Thus the Rayleigh number definition will be explored.

The thermal expansion coefficient presented in the definition of the Rayleigh number, Equation (47) is defined as:

$$\beta = \frac{1}{T_f} = \frac{2}{T_H + T_C} \tag{48}$$

where T_f is the film temperature used to define the temperature dependent properties. If Equation (48) is substitued into Equation (47), the resulting equation is:

$$T_H = T_C \left(\frac{d+1}{d-1}\right) \tag{49}$$

where

$$d = 2\,Ra\ \frac{\upsilon\,\alpha}{g\,L^3} \tag{50}$$

Equations (49) and (50) are then used to calculate the hot temperature by assuming the Rayleigh number, cold temperature, charactersitic length, and air properties.

Both studies [13, 17] had similar goals, but their respective models and conclusions differed. Chergui et al. [13] had a perpendicular junction to connect the chimney to the collector, while Tahar et al. [17] used a curved junction. Chergui et al. [13] found that the flow was laminar with a Rayleigh number of 10^6 and turbulent with a of 10^8, while Tahar et al. [17] found that the flow was laminar with a Rayleigh number of 10^3 and turbulent with 10^5. Along with the different geometries, different definitions of the characteristic length were used when calculating Rayleigh

numbers. Chergui et al. [13] used the total height of the system, *H*, as their characteristic length, while Tahar et al. [17] did not define their characteristic length. However, based on the work herein, it will be shown that most likely, Tahar et al. [17] used the average height of separation between the ground and chimney wall, *h*. Table 3.1 presents the hot temperatures applied to the ground and their respective Rayleigh numbers when defined using different characteristic lengths. When the characteristic length is *H*, *Ra* is greater than when the characteristic length is *h*, which explains why a Rayleigh number of 10^5 is laminar with one study but turbulent with the other. The following sections use the studies from Chergui et al. [13] and Tahar et al. [17] to further validate the modeling approachs that will be used to simulate a solar power plant.

Table 3.1: Rayleigh calculation cases

Case	Ra_H	Ra_h	T_C (K)	T_H (K)
1	3.26×10^4	100	290	290.0003
2	10^5	330	290	290.0009
3	2.93×10^5	1000	290	290.0027
4	10^6	3369	290	290.0092
5	2.96×10^6	10^4	290	290.0273
6	10^7	3.37×10^4	290	290.0922
7	2.96×10^7	10^5	290	290.2737
8	10^8	3.37×10^5	290	290.9287
9	2.96×10^8	10^6	290	292.7961

3.2.1. Solar Chimney with Perpendicular Junction

In 2010, Chergui et al. [13] modeled a solar chimney in a two-dimensional axisymmetric domain to investigate the effects of the Rayleigh number on the flow. The schematic for the system is presented in Figure 3.6a where the total height, *H*, of the system is 1 m. Chergui et al. [13] did

not specify many of the boundary conditions in their study, so the boundary conditions from Tahar et al. [17] are used. The outlet is modeled at 1 atm with a backflow temperature of T_C, and the inlet specifies zero velocity [13] and a temperature of T_C. Both the collector and tower are modeled as no-slip walls with temperatures of T_C, and the ground is modeled as a no-slip wall with a temperature of T_H. For the current study, the system is modeled with an axisymmetric domain assuming laminar and steady-state flow. The properties are defined by using Equation (48). The temperature difference between the ground and chimney drives the flow in natural convection, and different Rayleigh numbers are used to calculate a corresponding T_H.

A grid resolution study was conducted to determine the proper cell size to achieve grid-independent results. A uniform mesh with orthogonal cells was used, and a sample mesh is shown in Figure 3.7. The mesh was defined as $m \times n$ where m is the number of cells along the y and r axis and n is the number of cells along the inlet and outlet. Therefore, the total number of cells can be defined as:

$$N = 2\,m\,n \tag{51}$$

Three different meshes are tested; 200 × 20, 300 × 30, and 400 × 40, corresponding to N = 8000, 18000, and 32000, respectively. The axial velocity along the axis of symmetry is extracted to compare the effects from the grid resolutions. The extrapolated points at y = 0.1, 0.3, 0.5, 0.7 and 0.9 m using the grid resolution method are also included. The results are shown in Figure 3.8, for the case when Ra_H is 10^8. A turbulent case was chosen to ensure that cell size impacts the results as little as possible because the velocities vary more dramatically. For the axial velocity profile, beginning at the bottom, the velocity is 0 m/s and increases to a maximum at around y = 0.3 m, and then decreases higher in the tower. In addition, the coarse mesh appears to have lower vertical velocities than the two finer meshes and the extrapolated velocities align with both the

medium and fine mesh. From Equation (29), the GCI_{fine}^{21} values for the five y positions range from 0.01% - 0.76% indicating that the fine mesh accounts for a very small numerical error. The relative error between the medium and fine mesh are below 1% at all y positions, and therefore, the medium mesh, 300 × 40, is used going forward because it provides the best balance between the computer time required and numerical error.

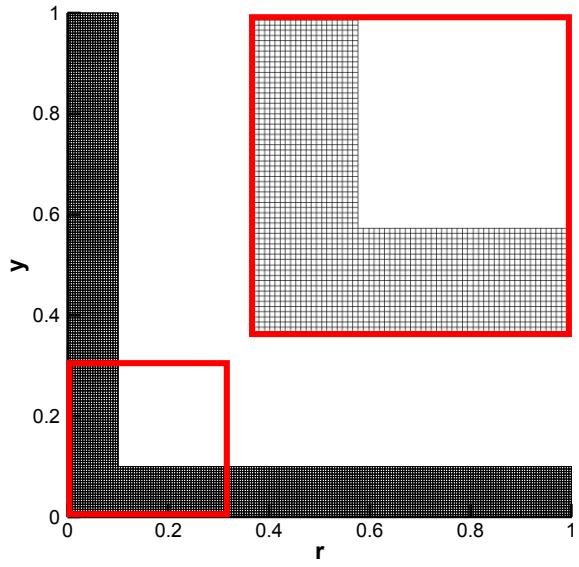

Figure 3.7: Generated mesh of solar chimney with perpendicular junction

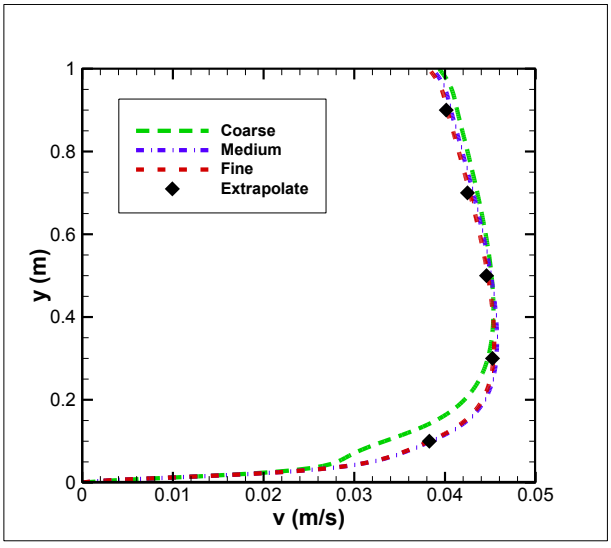

Figure 3.8: Grid resolution study for solar chimney with perpendicular junction; height versus vertical velocity along the axis

Figure 3.9 presents the dimensionless temperature contours for the current study for cases 2, 4, 6, and 8 (see Table 3.1). Beginning with cases where Ra_H is 10^5 and 10^6, the flow is laminar, and increasing the temperature difference $(T_H - T_\infty)$ increases the height of the dimensionless temperature near the centerline. When Ra_H is 10^7 and 10^8, the flow is turbulent, and as the temperature difference increases, the number of convection cells decreases. Similar to Chergui et al. [13], the flow is turbulent when Ra_H is 10^8 and laminar when Ra_H is 10^6.

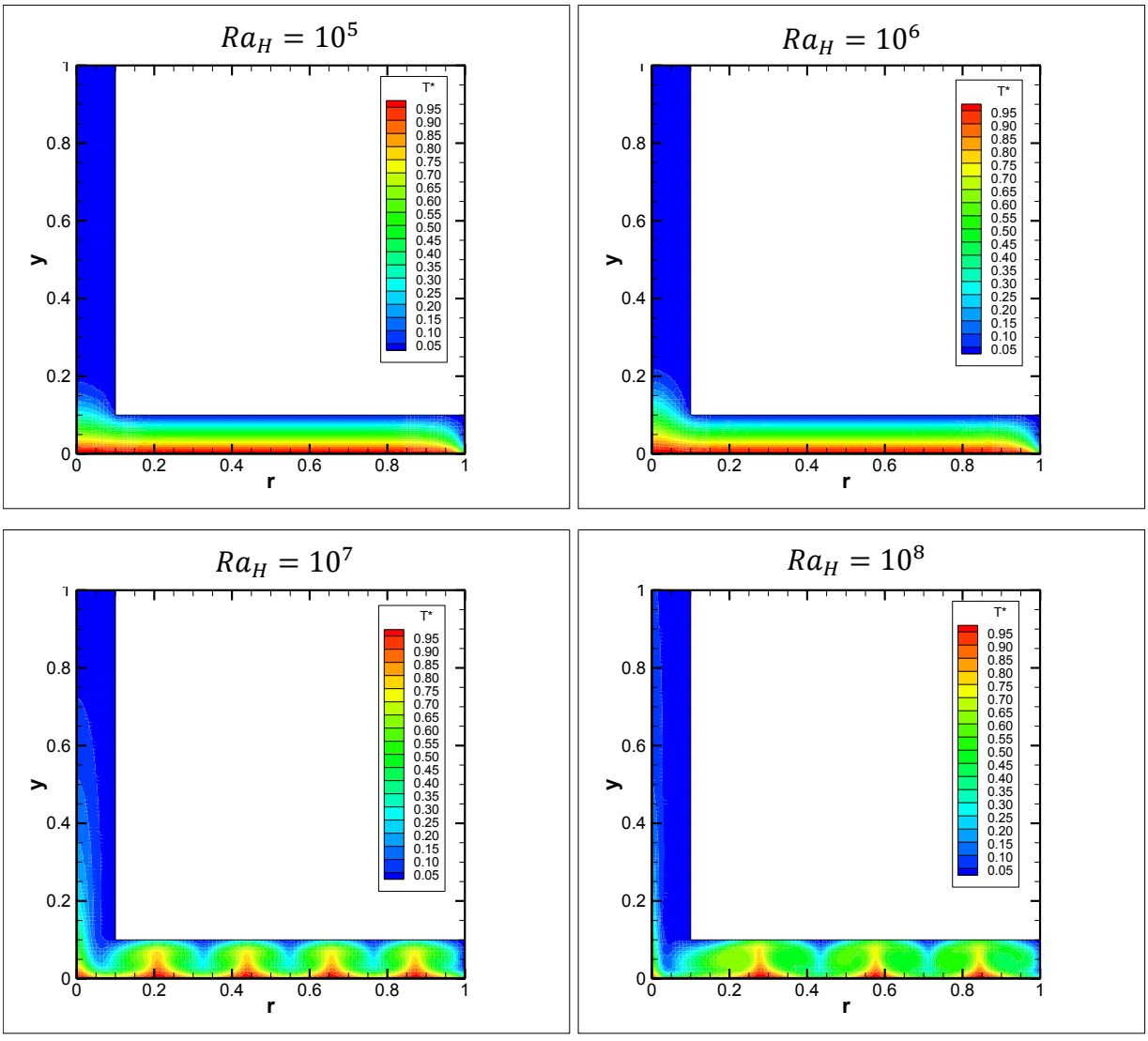

Figure 3.9: Dimensionless temperature contours for Rayleigh number comparison with the perpendicular junction solar chimney

3.2.2. Solar Chimney with Curved Junction

In 2012 and 2013, Tahar et al. [14, 17] used ANSYS Fluent to model a solar chimney in a two-dimensional axisymmetric domain to investigate the effects of the Rayleigh number on the flow. The schematic for the system is presented in Figure 3.6b where the average distance between the chimney and ground, h, is about 0.15 m. The geometry and boundary conditions chosen for the current study are the same as 3.2.1 but the chimney has a curved junction joining the collector to the chimney wall. The boundary conditions are shown in Figure 3.6b.

A grid resolution study was performed to determine the proper cell size and amount of nodes due to the presence of the curvature, which distorts the cell shapes. A non-uniform mesh was constructed and an example mesh is shown in Figure 3.10. Similar to before, the mesh was defined as $m \times n$ for a total of N cells defined in Equation (51). The finest cells are located at the inlet and outlet, and the coarsest cells are found along $y = x$.

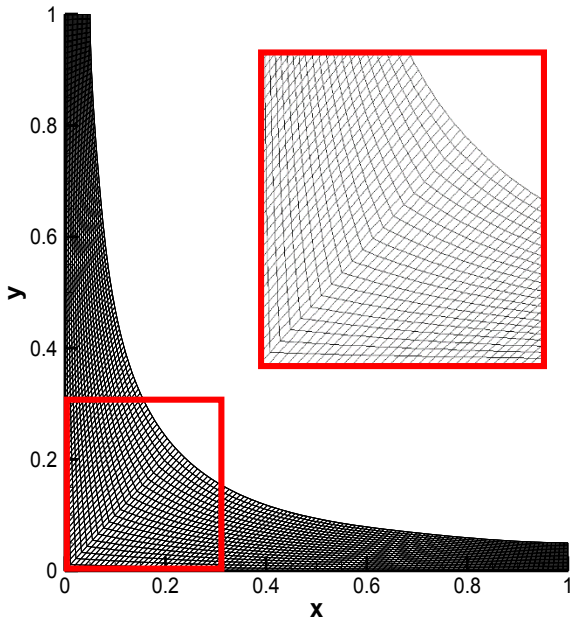

Figure 3.10: Generated mesh of solar chimney with curved junction

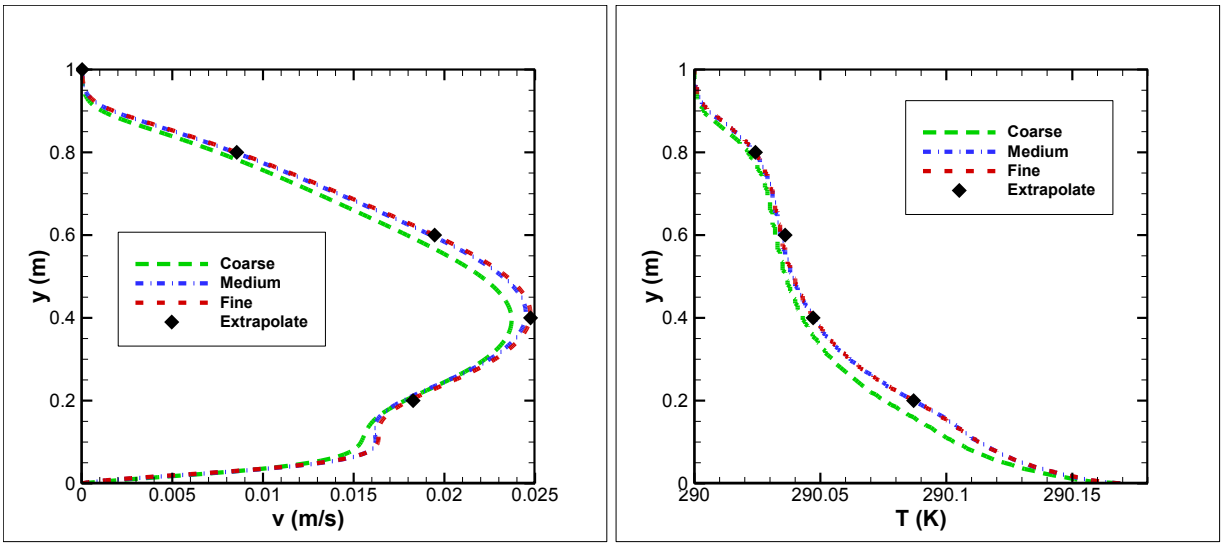

Figure 3.11: Grid resolution study of solar chimney with curved junction; height versus vertical velocity and temperature along the axis of symmetry

The grid resolution study is performed on three different meshes; 200 × 40, 300 × 60, and 400 × 80, corresponding to N = 16000, 36000, and 64000, respectively. For the study, the vertical velocity and temperature profiles along the axis are extracted to compare the effects from the different cell sizes. The property profiles along the axis and the extrapolated values at y = 0.2, 0.4, 0.6, and 0.8 m are shown in Figure 3.11, where the first plot is the vertical velocity and the second is the temperature for Ra_h 10^5. Beginning with the vertical velocity profile, the velocity begins at 0 m/s and increases to local maxima near y = 0.1 m, and then reaches a maximum near y = 0.4 m before decreasing to 0 m/s. Also, the coarse mesh appears to have lower velocities than the two finer meshes. The temperature decreases with increasing vertical direction, and like the vertical velocity profile, the coarse mesh has lower values than the finer meshes. The extrapolated values align with both the medium and fine mesh. The vertical velocity profile contains GCI_{fine}^{21} values varying from 0.04% - 0.14%, and the temperature profile contains GCI_{fine}^{21} values all below 0.01%

indicating that there is little numerical error with the fine mesh. The relative errors between the medium and fine meshes are below 0.1%, so the medium mesh, 300 × 60, is chosen going forward

Figure 3.12 presents the dimensionless temperature contours for the cases 1, 3, 5, 7, and 9, shown in Table 3.1. Beginning with cases when Ra_h are 100 and 1000, the flow is laminar, and as the hot temperature is increased (from Ra_h 100 to 1000), the maximum temperature near the center rises. When Ra_h is 10^4, the transition from laminar to turbulent flow can be observed. The flow is turbulent near the center where the separation height between the chimney and ground is the greatest and continues outward until the turbulent flow reaches the inlet. Finally when Ra_h = 10^5 and 10^6, the flow is fully turbulent and as the temperature difference continues to increase, the number of convection cells decreases. Overall, the results have the same conclusions as Tahar et al. [17], the flow is laminar when Ra_h is 10^3, and the flow is turbulent when Ra_h is 10^5. In addition, when Ra_h is 10^5, like Tahar et al. [17], there are four pairs of convection cells. Using Table 3.1 , Ra_h can be converted to Ra_H to represent the Rayleigh numbers from Chergui et al. [13]. The flow is laminar when $Ra_H = 3 \times 10^5$, and turbulent when $Ra_H = 3 \times 10^8$. The current model also reaches the same conclusions as Chergui et al. [13]. Therefore, the method of defining the characteristic length within the Rayleigh number calculation greatly impacts the transition value.

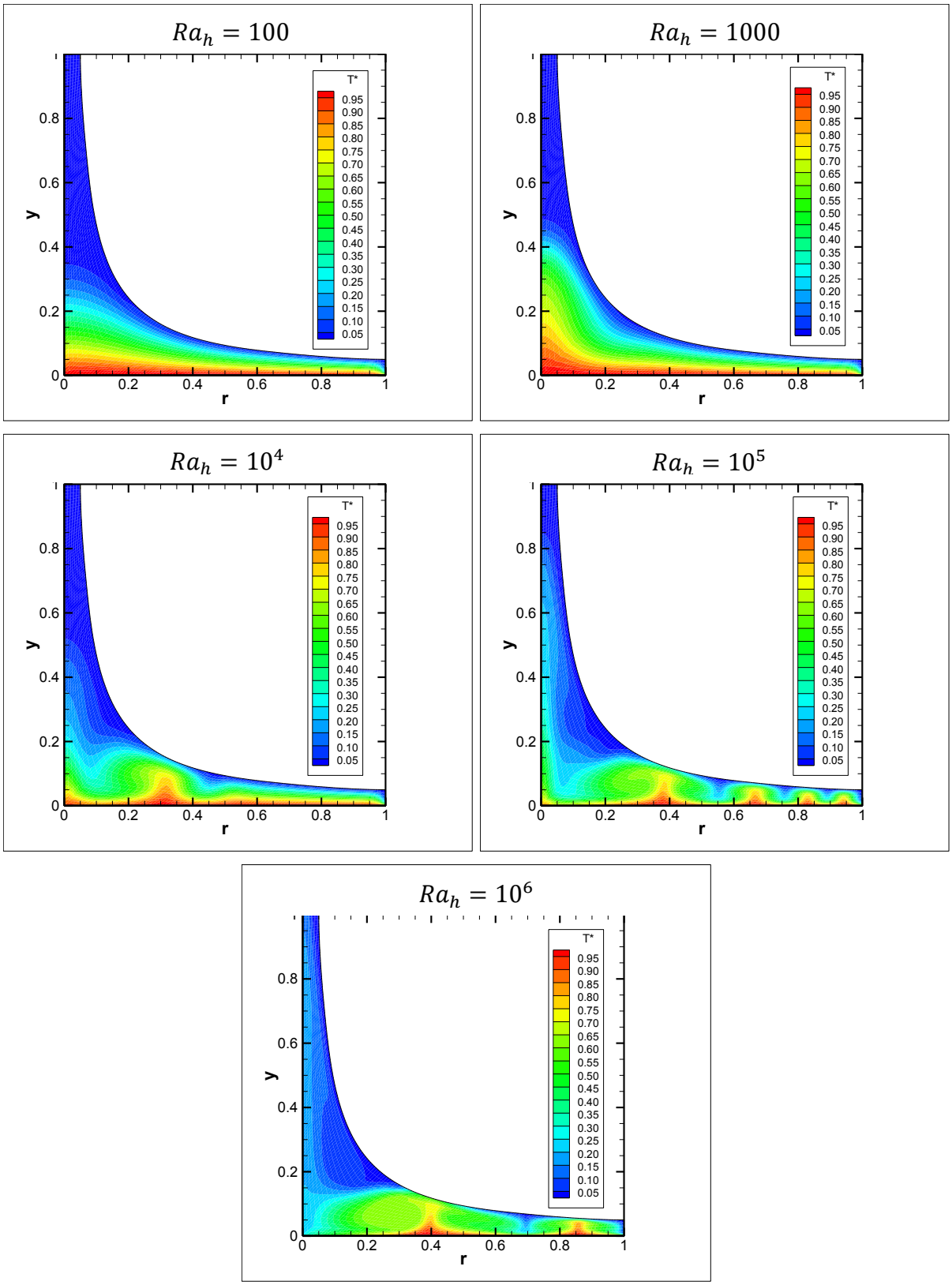

Figure 3.12: Dimensionless temperature contours for Rayleigh number comparison with the curved junction solar chimney

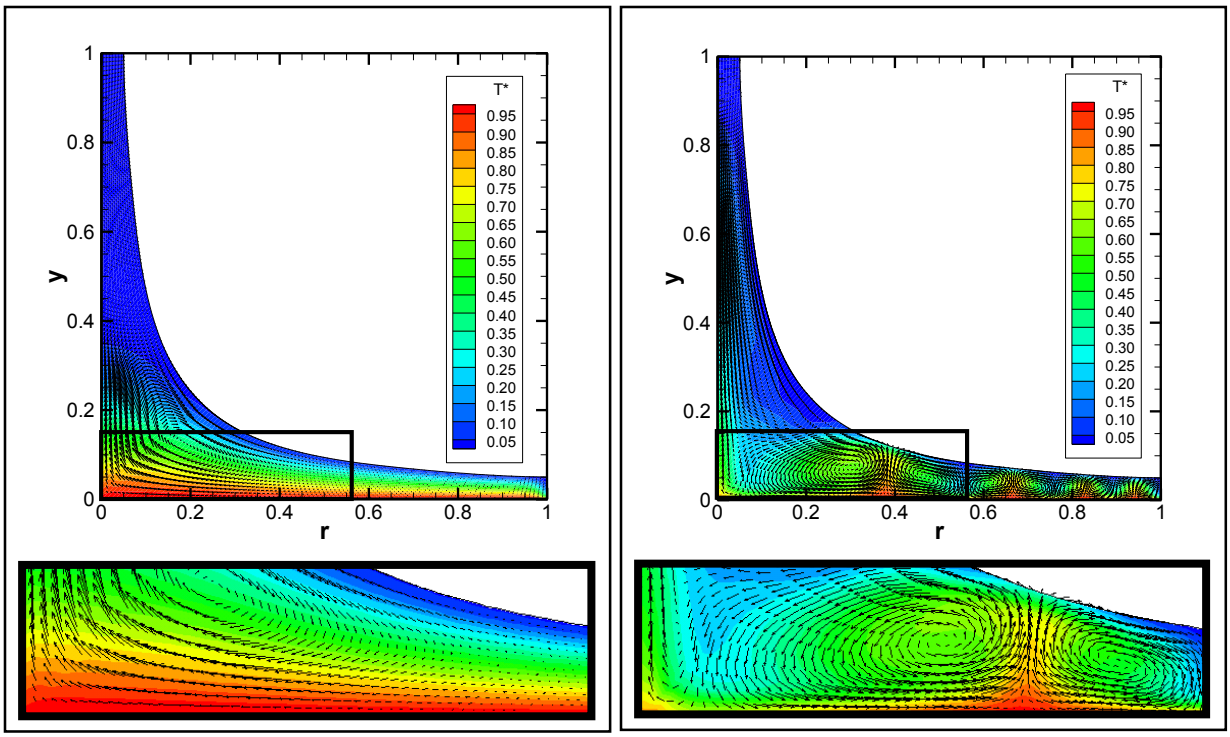

Figure 3.13: Dimensionless temperature contours with velocity vectors

Vector lines can help elucidate magnitude and direction of the flow within the system, and Figure 3.13 presents the dimensionless temperature contours overlaid with the velocity vectors. The contour on the left presents laminar flow when Ra_h = 100, where the air rises near the axis and circulates under the curvature of the collector. The figure on the right is turbulent flow when Ra_h = 10^5. For the turbulent flow, there are numerous convection cells where the air recirculates inside; thus the cells represent recirculation zones. Overall, Figure 3.13 provides more information on the fluid motion within the system caused by natural convection from the temperature difference between the ground and collector wall, and compares laminar and turbulent flow.

Tahar et al. [17] and Chergui et al. [13] both assumed laminar flow and did not use a turbulence model in their simulations. The current study investigates the effects of the standard and realizable *k*-ε turbulence models. Figure 3.14 shows the dimensionless temperature contours for the two

turbulence models of Ra_H equals 10^3 and 10^5. When the flow is laminar, the turbulence models predict the same solutions as the laminar case (first row and second column in Figure 3.12). When the flow is turbulent, the two models predict a different number of recirculation zones near the ground. From the position $r = 0.2$ to $r = 1$, the standard model has the same number of convection cells when assuming laminar flow (second row and second column in Figure 3.12), while the realizable model has one more.

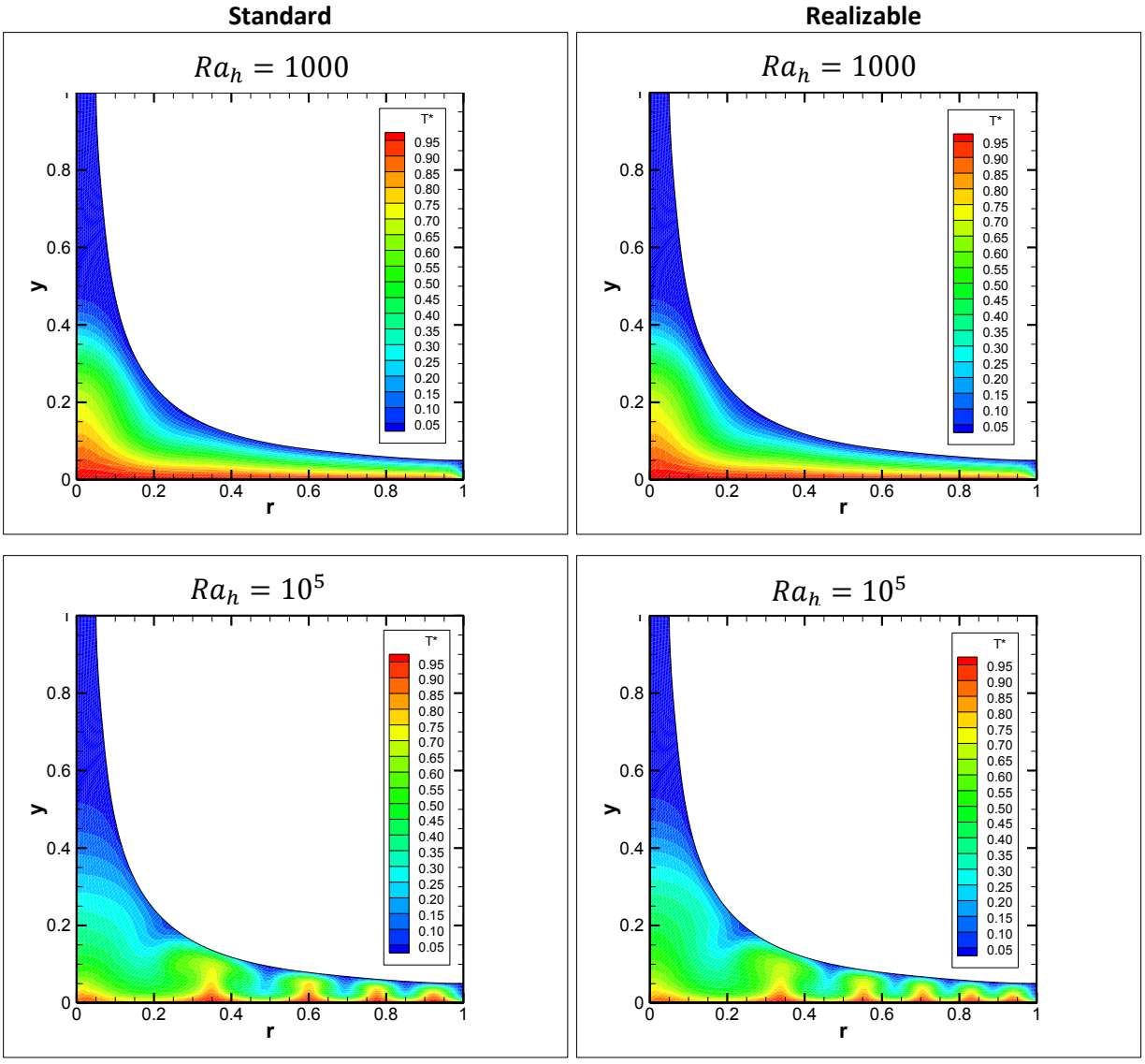

Figure 3.14: Dimensionless temperature contours with the standard and realizable *k-ε* turbulence models

3.3. Solar Chimney with Turbine Load and Energy Storage Layer

In 2010, Xu et al. [10] created a two-dimensional axisymmetric model of a solar updraft power plant that contained an energy storage layer, collector, turbine, and the chimney. The schematic is shown in Figure 3.15; the tower height is 200 m with a diameter of 10 m, the collector has an inclined height of 2 m at the inlet and 6 m before the bend, and a diameter of 122 m, and the energy storage layer (area between the ground top and ground bottom in Figure 3.15) has a thickness of 5 m. The boundary conditions used for the current study are the same as Xu et al. [10]. The ambient air temperature is 293 K. The collector is modeled with a convection boundary condition using a convection coefficient of h_c =10 W/(m^{2}K). The chimney and bend are both adiabatic no-slip walls. The bottom of the ground is a no-slip wall with a constant temperature of 300 K. Since the solar rays travel through the collector to heat the ground, a heat generation of 4 MW/m^3 is applied to the 0.1 mm thick top of the ground wall. Finally, a pressure drop of 120 Pa is used to model the turbine. Xu et al. [10] used a mesh of nearly 500,00 cells to ensure grid-independent simulation results, but the current study also investigates the grid resolution. The current study uses the realizable k-ε turbulence model. The temperature T_H is calculated by:

$$q_G" = h_c\,(T_H - T_C) \qquad (52)$$

where $q_G"$ is the energy released from the ground with units of W/m^2. In addition to the air properties, a solid soil material is defined with a density of 1700 kg/m^3, specific heat of 2600 J/(kg K), and thermal conductivity of 0.78 W/(m K) to model the thermal storage layer. The purpose of this validation is to better understand the methodology behind modeling the turbine and ground heat source, along with using a constant convection coefficient to represent the heat transfer between the surrounding air and collector.

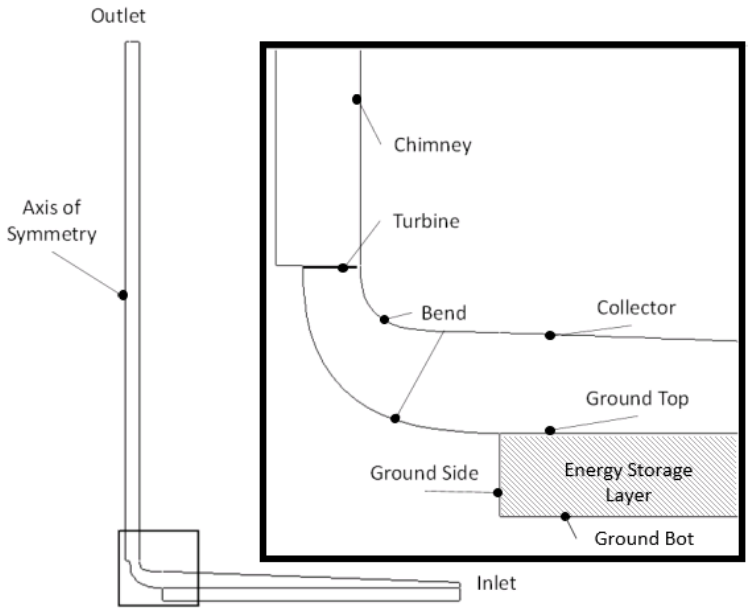

Figure 3.15: Schematic of solar chimney power plant model [10]

Like the previous validation studies, a grid resolution study was performed to ensure that grid independent results are achieved. The mesh is non-uniform as the cell size changes below the chimney and throughout the bend, but becomes uniform throughout the chimney. For the grid resolution study to compare cell size effects, three meshes are created; the coarse mesh has 38,680 cells, the medium mesh has 108,456 cells, and the fine meshes has 241,400 cells. The mesh with 241,400 cells is shown in Figure 3.16, where the figure focuses on a portion of the domain near the junction where the turbine is modeled.

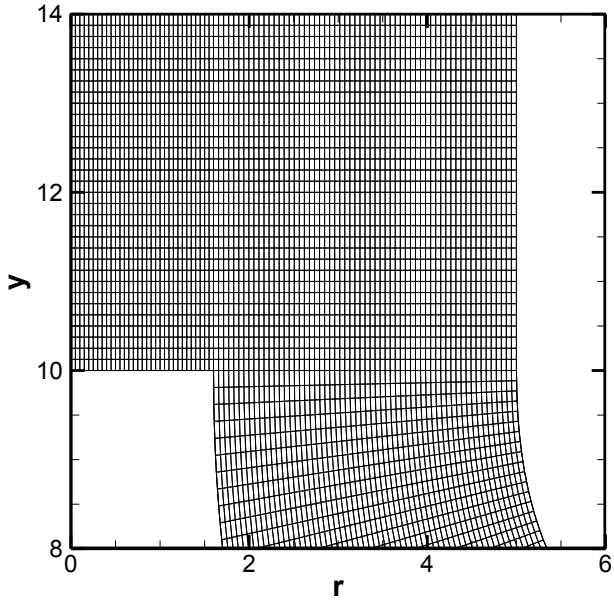

Figure 3.16: Mesh of solar chimney power plant model

The grid resolutions study was performed for the three different mesh sizes for the case where the ground heat generation is 4 MW/m^3 and the pressure drop is 0 Pa. Figure 3.17 presents the velocity and temperature profiles along the tower outlet along with extrapolated values from Equation (26). Beginning with the vertical velocity profile, the airflow is zero at the wall (x = 5 m) and increases to a maximum at the center (x = 0 m). For the temperature profile, values are relatively constant throughout the domain, but the center are slightly larger. The three meshes provide similar shapes and vertical velocity profiles, but the coarse mesh has a significantly different temperature profile. From Equation (29), the GCI_{fine}^{21} values vary from 0.03% to 0.37% for the vertical velocity profile and are all below 0.5% for the temperature profile. The relative error between the medium and fine mesh are all below 0.02%, and therefore, the medium mesh with 108,456 cells is used going forward.

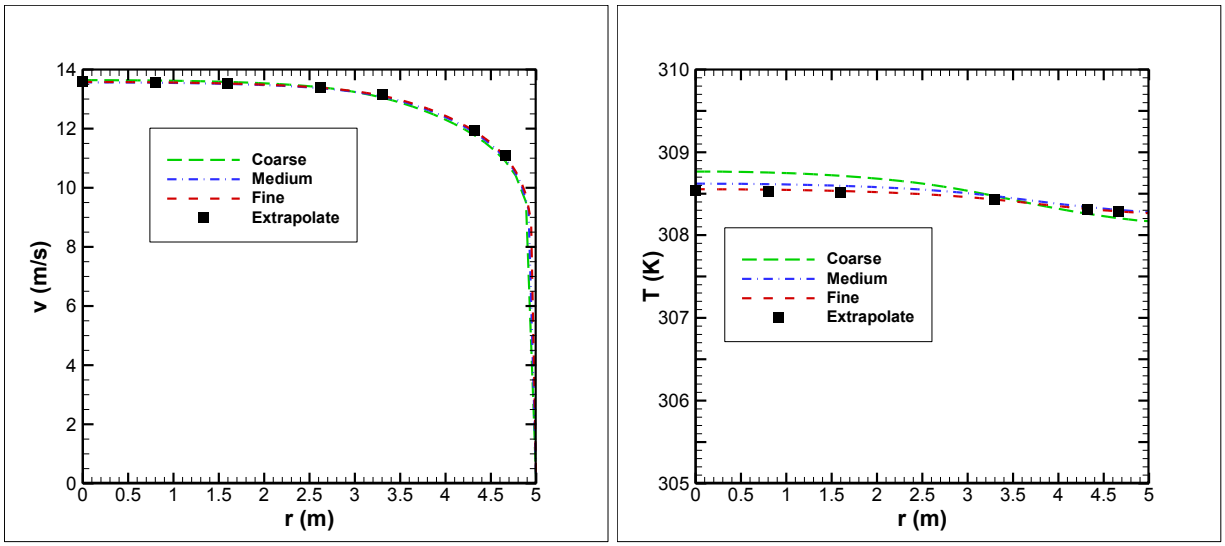

Figure 3.17: Grid resolution study for solar chimney; radius versus vertical velocity and temperature at the tower outlet

Xu et al. [10] modeled the solar chimney both with and without the turbine load. The current study uses the case where the heat generation is 4 MW/m^3 and pressure drop is 120 Pa to model the turbine, and compares those results to the findings from Xu et al. [10]. Without the turbine load (Δp_t = 0 Pa), the current simulation predicts an outlet velocity of 12.5 m/s and an outlet temperature of 308.4 K, while Xu et al. [10] found an outlet velocity of 13.5 m/s and an outlet temperature of 306 K. With the 120 Pa pressure drop, the current simulation predicts an outlet velocity of 7.9 m/s and outlet temperature of 316.4 K, while Xu et al. reported an outlet velocity of 9.5 m/s and an outlet temperature of 310 K [10]. The current methodology in modeling the turbine and collector is sufficient going forward because the discrepancies between the two studies are low and the impacts from the pressure drop appear consistent.

Xu et al. [10] used a 1 mm thick wall with a heat generation and solid energy storage layer below the ground to model the energy put into the system. A study is performed to see if the energy storage layer is necessary for modeling the power plant, and to compare predictions using

other models such as heat generation and heat flux boundary conditions. Three different models are compared. Model #1 contains the energy storage layer, while model #2 and #3 do not. Model #1 and #2 implement the heat generation boundary condition, while model #3 uses a heat flux no-slip wall. Theoretically, the heat generation and heat flux models should predict the same values as both specify the same amount of energy into the system. Table 3.1 presents the findings from the study. The values from models #2 and #3 are very similar, which indicate that the boundary conditions of heat generation and heat flux have little impact on the prediction. Also, the energy storage layer slightly decreases the velocity and raises the temperature, but the impact is not dramatic. Model #1 requires a more complex geometry and mesh than the other two due to the solid energy storage layer, which increases the computational run time. While models #1 and #2 represent the same thing, the heat flux boundary condition, model #2, was chosen to be used going forward in the following chapter.

Table 3.2: Different Ground Model Comparison

Variables	Model #1	Model #2	Model #3
v_o (m/s)	12.5	13.2	13.1
T_o (K)	308.4	309.0	309.0

Chapter 4. Solar Chimney Power Plant

4.1. Analytical Model

The goal of this work is to determine an appropriate way to model the solar chimney to predict the energy output with a turbine without modeling the actual turbine. The modeling of the turbine can be achieved by specifying a pressure drop that would equate to the actual performance, as reported by Xu et al. [10]. Therefore, the approach herein will be to first model the chimney without a turbine load and validate the results with published literature. Then, the turbine load will be modeled and further studies will be presented. Finally, a study on the effects of the turbine will be presented including a way to create a predictive equation for the output. The analyses will be used to determine if it is possible to create an efficient solar chimney power plant while also reducing the tower height.

4.1.1. Maximum Velocity without Turbine Load

The solar chimney is analyzed to determine the maximum velocity that the air can theoretically travel through the tower due to solar radiation. The tower converts the heat produced by the collector into kinetic energy, therefore, the density difference caused by the increase in temperature within the collector works as the driving force. The air within the tower is lighter than the air at the outlet, which causes buoyancy. Without the turbine, the theoretical power that can be achieved by the flow in the tower, P_{tower}, is defined using the kinetic energy [4]:

$$\mathcal{P}_{tower} = \frac{1}{2}\dot{m}\, {v_{nt}}^2 \qquad (53)$$

and the equation based on the pressure difference between the bottom of the tower and ambient air at the tower exit [4] can be expressed:

$$\mathcal{P}_{tower} = \Delta p_{tower}\, v_{nt}\, A_{tower} \quad (54)$$

where v_{nt} is the velocity at the entrance of the tower and A_{tower} is the cross-sectional area at the tower outlet. The pressure difference in Equation (54) is expressed as:

$$\Delta p_{tower} = g\, H\, (\rho_\infty - \rho_{tower}) \quad (55)$$

where H is the height of the tower [4]. If Equations (53) and (54) are set equal to each other along with substituting Equation (55) and the Bousinessq approximation (Equation (6)), the form of v_{nt} is:

$$v_{nt} = \sqrt{2\, g\, H\, \frac{\Delta T}{T_\infty}} \quad (56)$$

where $\Delta T = T_t - T_\infty$ and T_t is the average temperature within the tower. Equation (56) is used to represent the velocity entering the tower without the turbine load and is proportional to the square root of the tower height and temperature difference.

4.1.2. Maximum Power Output

The solar chimney is now analyzed to determine the maximum power output due to solar radiation received by the collector. According to Schlaich [4], the power output from the turbine is:

$$\dot{W}_t = \dot{Q}_s\, \eta_t\, \eta_{collector}\, \eta_{tower} \quad (57)$$

where the η variables represent the efficiencies of the turbine, collector, and tower, respectively. $\dot{Q}_s$ is the amount of energy into the system through the collector from the sun, which is:

$$\dot{Q}_s = A_{collector} q_S'' \quad (58)$$

where $A_{collector}$ is the cross-sectional area of the collector top surface and q_S" is the global horizontal solar radiation. Therefore, to solve Equation (57), the efficiencies of the collector and tower are required.

The efficiency of the collector represents the energy received by the collector to the total solar radiation to the system. The collector efficiency is defined as:

$$\eta_{collector} = \frac{\dot{Q}_{collector}}{\dot{Q}_S} \quad (59)$$

where $\dot{Q}_{collector}$ is the heat transfer below the collector and expressed as:

$$\dot{Q}_{collector} = \dot{m}\, c_p\, \Delta T \quad (60)$$

If Equations (58) and (60) are substituted into (59), the collector efficiency can be calculated as:

$$\eta_{collector} = \frac{\rho\, v_{nt}\, A_{tower}\, c_p\, \Delta T}{A_{collector}\, q_S"} \quad (61)$$

Equation (61) shows that the temperature difference and cross-sectional area of the tower are inversely related.

The efficiency of the tower represents the kinetic energy of air in the tower versus the heat transfer at the base, and therefore, expressed as:

$$\eta_{tower} = \frac{\mathcal{P}_{tower}}{\dot{Q}_{tower}} \quad (62)$$

The heat transfer at the base is represented by:

$$\dot{Q}_{tower} = \dot{m}\, c_p\, \Delta T \quad (63)$$

If Equations (53), (56), and (63) are substituted into Equation (62), then the efficiency of the tower is simplified:

$$\eta_{tower} = \frac{g\ H}{c_p\ T_\infty} \tag{64}$$

where the tower efficiency is determined by the height of the tower and ambient air temperature. Theoretically, increasing the tower height increases the tower efficiency, and increasing the ambient temperature decreases the tower efficiency.

Substituting Equations (61) and (64) into Equation (57) results in the relationship for the turbine power output:

$$\dot{W}_t = \frac{1}{2}\ \pi\ \eta_t\ \rho\ v^3\ {r_{tower}}^2 \tag{65}$$

where tower efficiency is in terms of velocity. According to Haaf et al. [15] for the Spanish prototype, when the peak power output from the turbine is achieved, the vertical air velocity across the turbine is about 0.8 of the maximum velocity without the turbine load. Therefore, Equation (65) can be manipulated by substituting Equation (56) multiplied by 0.8. The resulting equation is:

$$\dot{W}_t = \frac{1}{2}\ \pi\ \eta_t\ \rho \left(0.8\ \sqrt{2\ g\ H\ \frac{\Delta T}{T_\infty}} \right)^3\ {r_{tower}}^2 \tag{66}$$

where ΔT is the temperature difference without the turbine. In addition, Pastohr et al. [9] used the Betz power limit, $16/27$, to calculate the peak pressure drop. If Equation (66) is multiplied by the Betz limit, the power output of the turbine can be expressed:

$$\dot{W}_t = \frac{8}{27}\,\pi\,\eta_t\,\rho\left(0.8\sqrt{2\,g\,H\,\frac{\Delta T}{T_\infty}}\right)^3 {r_{tower}}^2 \qquad (67)$$

Equations (66) and (67) are analytical relationships to calculate the maximum power output of a designated solar chimney knowing the tower height and radius, and temperature difference without using the actual characteristics of the turbine.

4.2. Heat Transfer

The relationship for the interaction between solar radiation and ground radiation exchange within the solar chimney was determined using an energy balance on the ground. Figure 4.1 is a schematic of the ground and the energy modes considered. The solar radiation absorbed by the ground is $\alpha_S\,q_S''$ and the emissive power from the ground is $E_G = \varepsilon_G\,\sigma\,{T_H}^4$ where ε_G is the ground emissivity is and σ is the Stefan Boltzmann constant. Also included is the convective heat transfer q_G'' (see Equation (52)). Assuming that the energy into and out of the ground is balanced, the resulting relationship is:

$$\dot{E}_{in} = \dot{E}_{out} \qquad (68)$$

$$\alpha_S\,q_S'' - \varepsilon_G\,\sigma\,{T_H}^4 - h_c\,(T_H - T_c) = 0 \qquad (69)$$

For the simulations, the absorptivity α_S = 0.95 [20] and the ground emissivity is ε_G = 0.575 [21] for summer months.

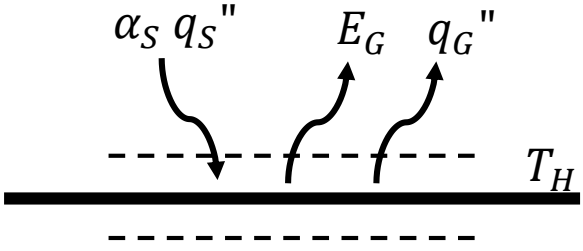

Figure 4.1: Schematic of heat transfer below the collector

4.3. Numerical Model

A numerical model of the solar chimney power plant is created in a two-dimensional axisymmetric domain with the numerical methods investigated in the validation cases: pressure-based solver with the SIMPLE method, realizable k-ε turbulence model, second-order upwind spatial discretization and first-order time discretization. The schematic for the current model is shown in Figure 4.2. The dimensions of the prototype and the environmental conditions used are similar to that of the Spanish prototype in Manzanares. The tower has a height of 195 m and diameter of 10 m, the collector has a height of 1.7 m and diameter of 240 m, and the turbine is placed within the tower at a height of 10 m. The average ambient temperature at the location of the prototype is about 20˚C, so the ambient temperature for the model is 293 K. The boundary conditions are similar to the ones from Xu et al. [10]. The collector is modeled as a convection boundary condition with a convection coefficient of 10 W/(m^{2}K). The chimney and bend are both adiabatic no-slip walls. To model the solar rays traveling through the collector to heat the ground and air, varying heat fluxes are applied to the ground boundary condition. The peak solar radiation, q_S", during the summer months in Manzanares, Spain is about 1000 W/m^2 and using Equation (69) results in a ground heat flux, q_G", of about 500 W/m^2. Therefore, realistic ground heat fluxes are chosen to be 400, 500, and 600 W/m^2. Finally, different pressure drops from 0 – 320 Pa are used to model how the turbine affects the flow.

The mesh used for the solar chimney power plant is shown in Figure 4.3 and contains 109,920 cells. The domain is magnified from 0 to 6 m along the r-axis and 6 to above 11 m along the y-axis to show the cells near the location of the turbine. The mesh is non-uniform and the sizes of the cells are finer below the collector, gradually increase through the bend, and are the coarsest inside the tower.

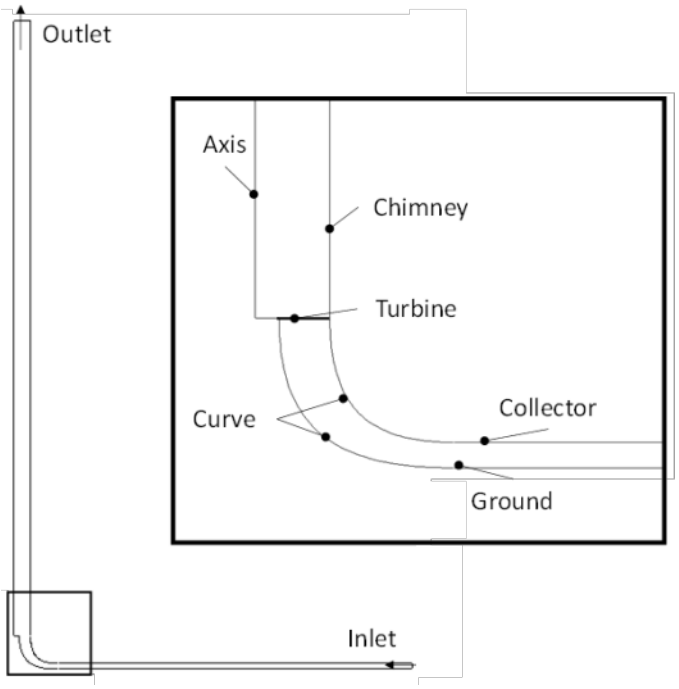

Figure 4.2: Schematic of solar chimney power plant

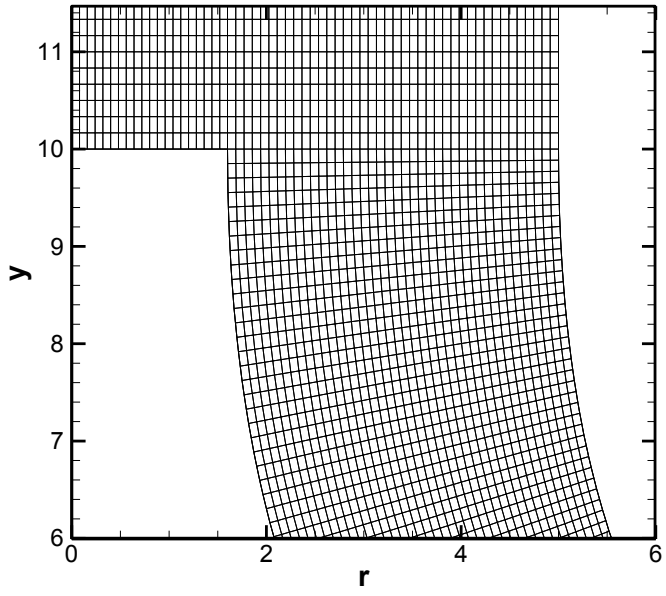

Figure 4.3: Mesh of solar chimney power plant model

The average outlet velocity and temperature at the outlet are extracted from the simulation. The work is then calculated:

$$\dot{W}_t = \Delta p_t \, \pi \, {r_{tower}}^2 \, v_0 \qquad (70)$$

where $\Delta p_{turbine}$ is the pressure drop that represents the turbine work and v_0 is the outlet velocity. The outlet velocity and tower radius are used becuase the volumetric flow rate is contant throughout the system. Equation (70) has a turbine efficiency of unity because the turbine effects are assumed in the definition of the pressure drop across the turbine. Therefore, the pressure drop represents the work extracted from the system.

The numerical model is designed to represent the prototype built in Spain. Table 4.1 shows the comparison between the tower inlet vertical velocity and temperature difference between the tower and ambient conditions for the simulation results and the data from the prototype [15] when there is no turbine load. When the solar radiation is 1000 W/m^2, the Spanish prototype reaches a vertical velocity of 15 m/s and a temperature difference of 20 K [15]. With the numerical model, the vertical velocity is 14.7 m/s with a temperature difference of 19.7 K. Overall, the relative errors are very small concluding that the simulation properly models the solar chimney without the turbine load.

Table 4.1: Comparison of simulation results to prototype data without turbine

Spanish Prototype			**Simulation**			**Relative Error**	
q_s'' (W/m^2)	v_{nt} (m/s)	ΔT (K)	q_G'' (W/m^2)	v_{nt} (m/s)	ΔT (K)	v_{nt}	ΔT
1000	15	20	500	14.68	19.7	2.1%	1.5%

After replicating the tower built in Manzanres without the turbine, the effects from the turbine were investigated. Table 4.2 compares the numerical predictions to the experimental data with the turbine load. When the solar radiation is 1000 W/m^2, the vertical velocity across the

turbine would reach 12 m/s resulting in a power output of 50 kW [15]. With the numerical model, a vertical velocity at the turbine is 11.96 m/s for a turbine pressure drop of 60 Pa. In addition, when the predicted velocity and pressure drop are substituted into Equation (70), the power output is 50.65 kW. In conclusion, the current model accurately represents the Spanish solar chimney both with and without the turbine and these two specific cases are used to invesigate.

Table 4.2: Comparison of simulation results to prototype data with turbine

Spanish Prototype			**Simulation (Δp_t = 60 Pa)**			**Relative Error**	
q_s" (W/m^2)	v_t (m/s)	$\dot{W}_t$ (kW)	q_G" (W/m^2)	v_t (m/s)	$\dot{W}_t$ (kW)	v_t	$\dot{W}_t$
1000	12	50	500	11.96	50.65	0.3%	1.3%

The pressure, temperature, and vertical velocity contours for the numerical model with a ground heat flux of 500 W/m^2 are shown in Figure 4.4. Examining the pressure, the values decrease under the collector toward the chimney, then reach the lowest value at the bend, and finally increase up the tower. The pressure drop represents a small change in kinetic energy locally near the turbine. The temperature distribution is very similar without and with the turbine model but the temperatures with the turbine model are about 4 K higher. The highest temperatures are found near the ground, bottom of the bend, and axis, and the overall temperatures increase with the inclusion of the turbine. The vertical velocity contours present the air flow as it travels up the tower, and similarly to the temperature contours, the shapes remain the same, but the velocities decrease with the pressure drop. The maximum vertical velocity is found at the location of the turbine where the pressure is the lowest. Right above the turbine and near the axis, air recirculates, shown as negative velocities. In conclusion, the turbine boundary condition accounts for the work extracted from the system, and increases the temperatures and decreases the velocities within the system.

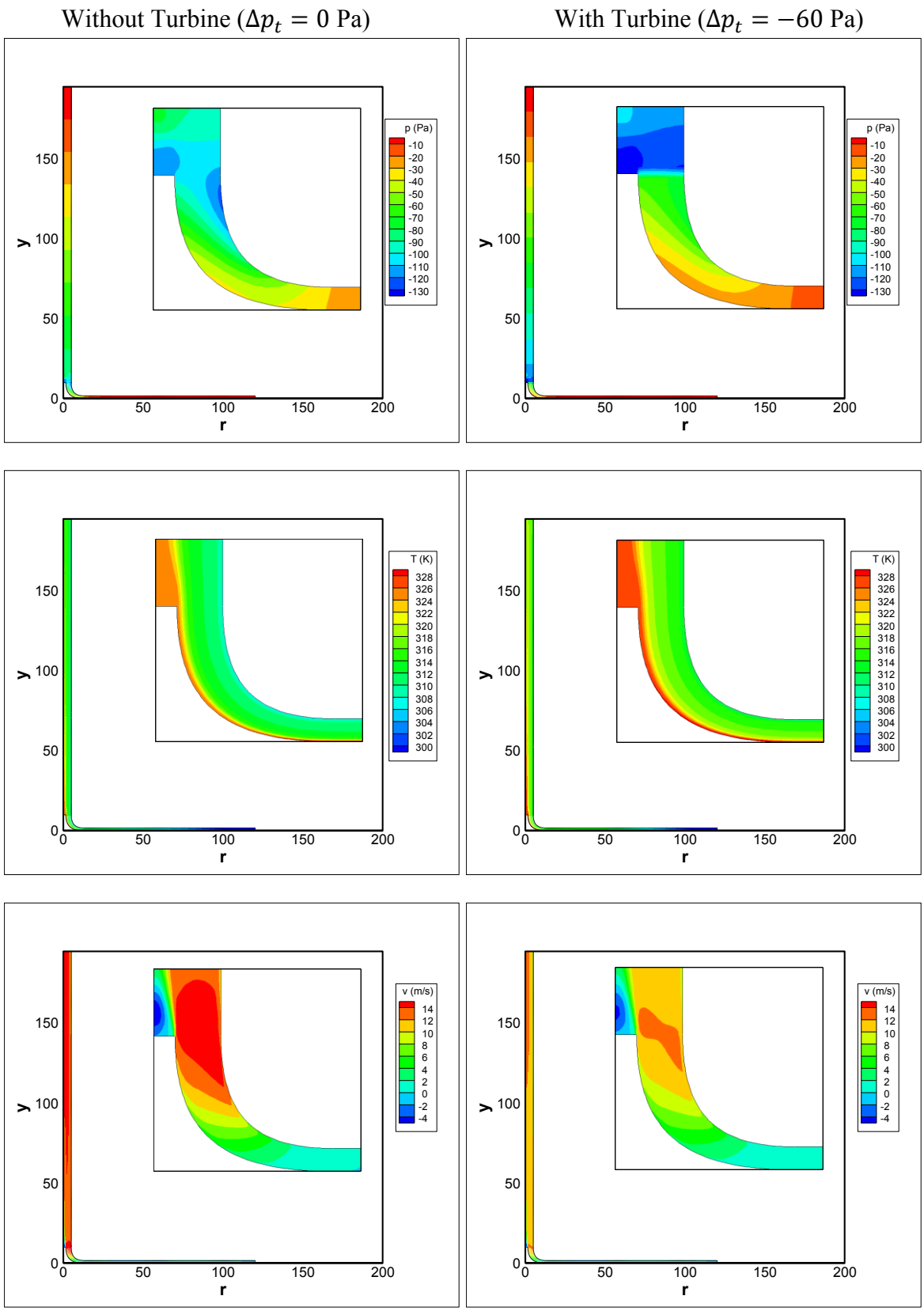

Figure 4.4: Numerical contours of pressure, temperature, and velocity without and with the turbine load

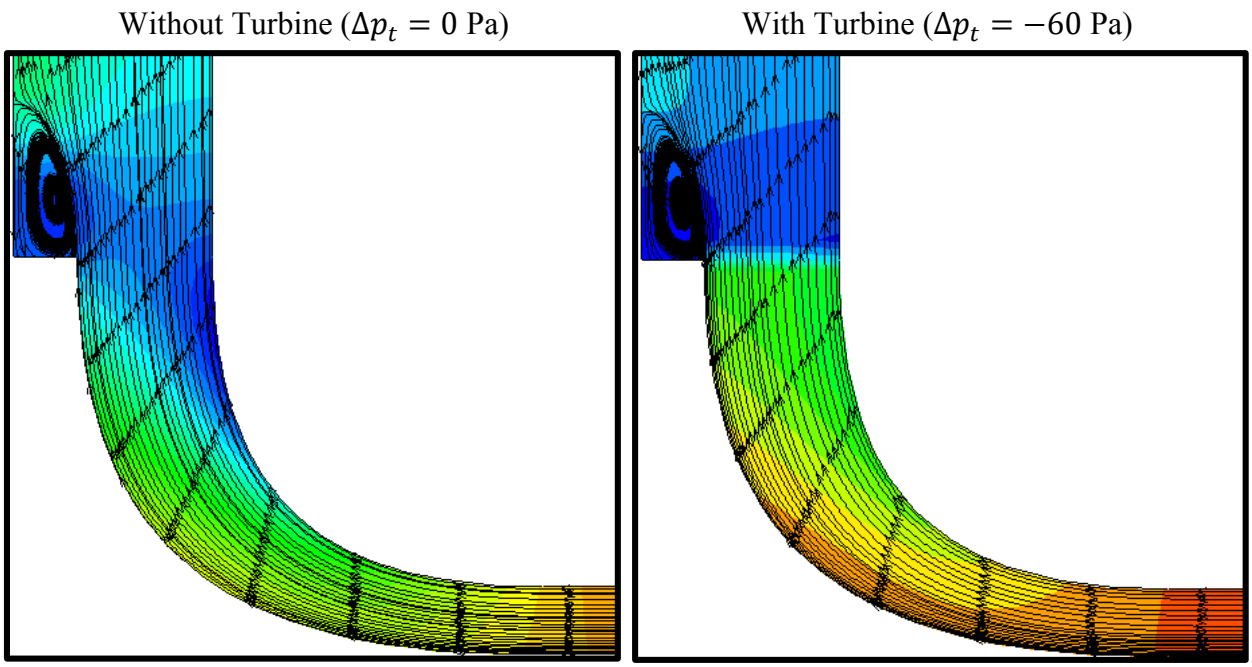

Figure 4.5: Pressure contours overlaid with streamlines for solar chimney with and without the turbine

In addition to the contours, streamlines provide a way to visualize the airflow within the system. Figure 4.5 presents the pressure contours from Figure 4.4 overlaid with streamlines when the pressure drop is 0 Pa and 60 Pa. The domain is magnified to better show the flow through the bend and across the turbine. The streamlines show that the flow travels under the collector toward the axis and then up the tower. Also the air circulation near the axis above the chimney inlet is visible.

The airflow below the collector behaves differently than the air inside the tower because it is constantly being heated as it flows toward the chimney. Figure 4.6 presents the temperature and horizontal velocity profiles in-between the ground and collector wall at a height of 0.85 m. The temperatures remain equal to the ambient temperature for a couple of meters and then increase continually as the airflow moves to the center, and the temperatures below the collector increase

with the inclusion of the turbine load. The horizontal velocity increases as the air approaches the center, and the turbine decreases the overall horizontal velocity values below the collector.

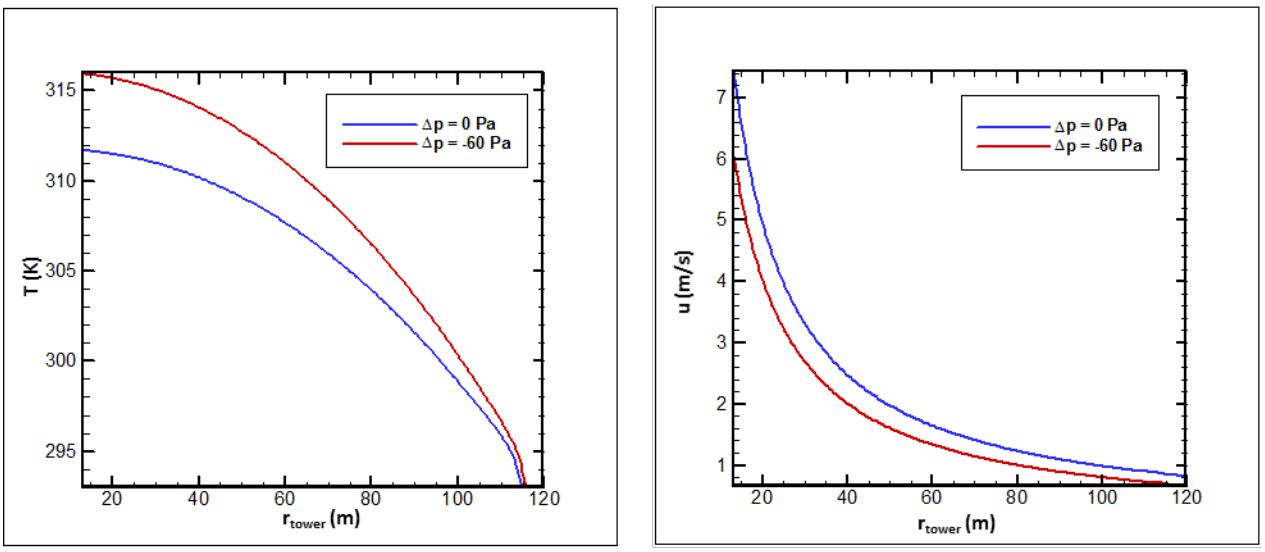

Figure 4.6: Temperature and horizontal velocity vs tower radius at a height of 0.85 m

4.4. Vertical Turbines versus Horizontal Turbines

The goal of the next study is to investigate if the location of the turbine affects the power output of the system. EnviroMission is in the process of designing a solar chimney power plant to be built with thirty-two smaller horizontal turbines near the center and below the collector as opposed to one vertical turbine at the bottom of the tower used by the prototype in Manzanares, Spain [3]. The schematics of the two turbine systems are presented in Figure 4.7. The vertical turbine harnesses the vertical flow while the horizontal turbine harnesses horizontal airflow.

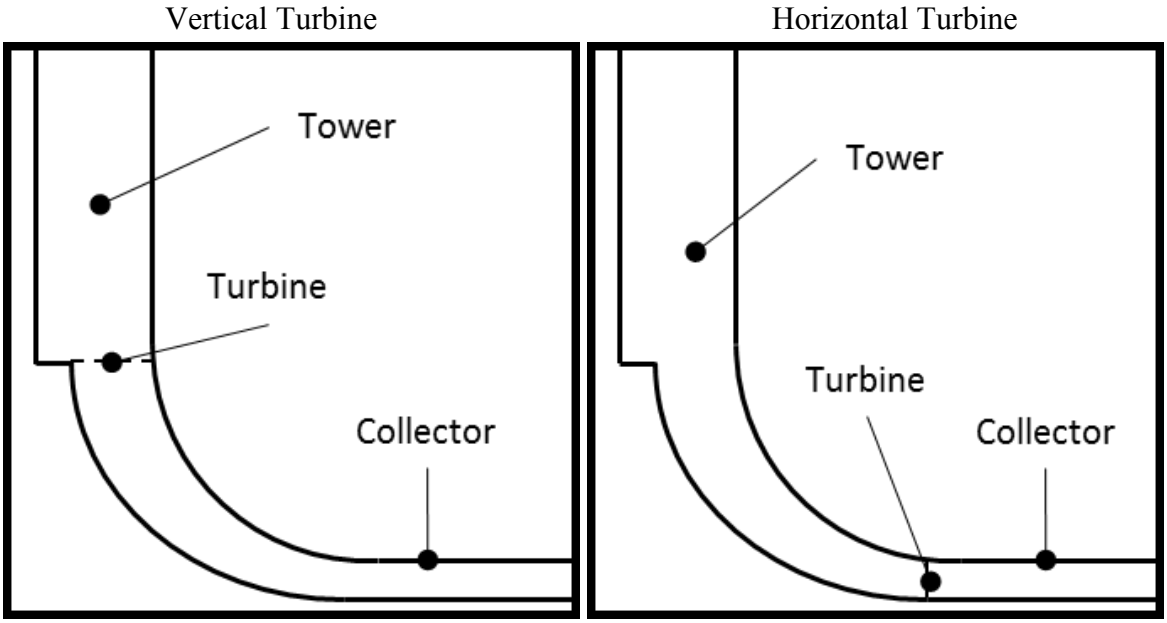

Figure 4.7: Schematics for vertical and horizontal turbine models

Table 4.3 presents the data extracted from the two different turbine models over numerous turbine pressure drops. Both turbine models predict very similar results. The table indicates that the turbine location does not alter the velocities and temperatures within the system and that other factors should be considered when selecting the location within the system to place the turbine. To improve the power output, the turbine(s) should be selected that have higher efficiencies or are able to increase the maximum pressure drop. In addition, other major factors in choosing the proper location for the turbine(s) are monetary, safety, and accessibility. For example, since increasing the tower diameter increases the power output, there may be a system where many smaller turbines are more cost effective than a single larger turbine.

Table 4.3: Vertical and horizontal turbine comparison

	Vertical Turbine		Horizontal Turbine	
Δp_t (Pa)	v_o (m/s)	T_o (K)	v_o (m/s)	T_o (K)
0	13.20	312.6	13.20	312.6
40	11.56	315.2	11.54	315.2
80	9.96	318.5	9.92	318.5
120	8.48	322.5	8.43	322.6
160	7.17	327.3	7.12	327.5

4.5. Further Comparisons of Spanish Prototype and Numerical Models

Without the turbine load, the velocity at the bottom of the tower can be calculated from the analytical model (Equation (56)) and extracted from the numerical model to be compared to the experimental data take from the Spanish prototype [15]. Figure 4.8 shows the curve comparing the analytical and numerical models to the experimental data by plotting the vertical velocity to the respective temperature difference within the tower. The predictions are from the numerical simulation with ground heat fluxes of 200, 300, 400, 500, and 600 W/m^2, and the data from the prototype is measured when the solar radiation was 800 and 1000 W/m^2. The simulated and experimental data align with the analytical curve very well. Both the analytical and simulated curves have the shape of a square root function. From Figure 4.8, both the analytical and simulated models successfully represent the Spanish solar chimney power plant when the turbine is not present.

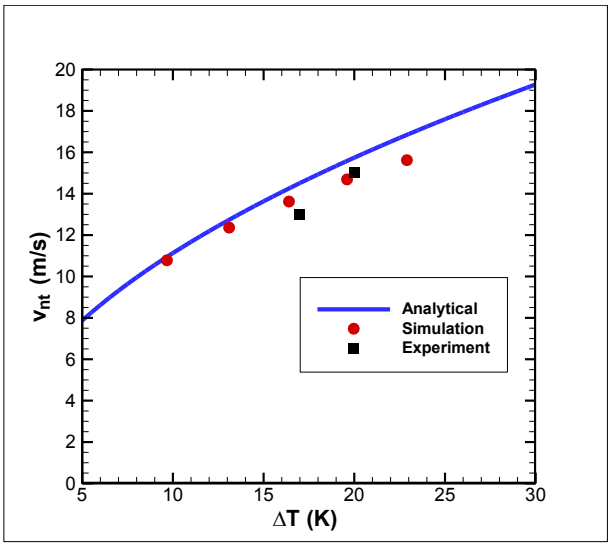

Figure 4.8: Vertical velocity versus temperature difference with no turbine load

Recall that Equations (66) and (67) are the analytical models for the maximum power output produced from the solar chimney, and the difference is the Betz power limit. According to Xu et al. [10], a turbine power output higher than the Betz power limit can be achieved, but it is still used as a predictive value reported by Pastohr et al. [9]. Figure 4.9 presents the two analytical curves along with both the simulated and experimental data comparing the maximum power output for different temperature differences. The simulation and experimental power outputs are very similar and both are in-between the two analytical curves, where the analytical power output using the Betz limit (Equation (67)) is below the data. Figure 4.9 provides evidence that both the numerical and the analytical models are accurate in modeling the solar chimney power plant with the turbine. The analytical model without the Betz limit will be used to investigate the geometric effects on the flow, following the recommendations from Xu et al. [10].

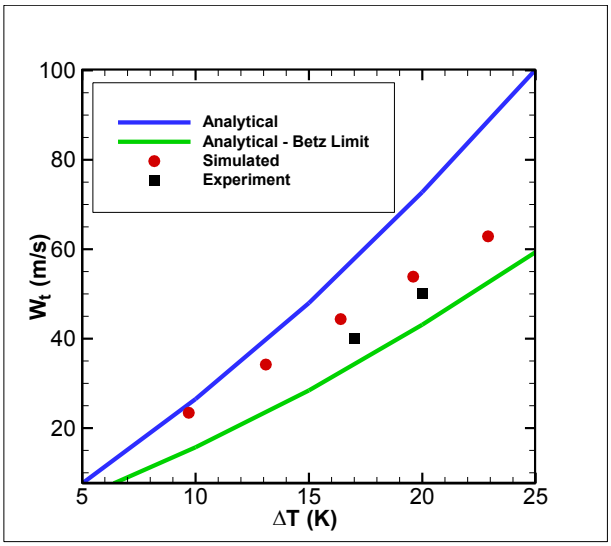

Figure 4.9: Maximum turbine power output versus temperature difference with a turbine load

4.6. Geometry Effects

The analytical models have been shown to successfully represent the solar updraft tower built in Spain and can be used to determine the effects that different system sizes have on the airflow and power output. Beginning with the model without the turbine, Figure 4.10 presents the curve from Equation (56) showing the vertical velocity when altering the height of the tower for different temperature differences. The curves take the shape of a square root function, such that as the height of the tower increases, so does vertical velocity.

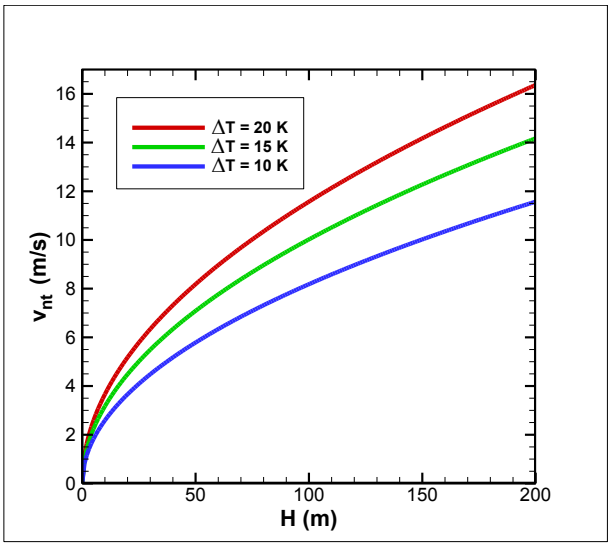

Figure 4.10: Vertical velocity versus height without a turbine load

From Equation (66), both the tower height and diameter impact the power output from the system. Figure 4.11 shows the curves of the power output when varying *H* and *D*, respectively, for three temperature differences. The base case is selected from the Spanish solar chimney and has a tower height of 185 m and diameter of 10 m. Increasing the temperature difference, tower height, and tower diameter all increase the power output from the turbine. The curves have the shape of a cubed function, which indicates that the impacts on the power output are more significant as the height and diameter are increased. Notably from Equation (61), the temperatures within the system and tower diameter are inversely associated such that increasing the tower diameter would result in a lower temperature difference. In conclusion, increasing the system size significantly increases the overall power output, but the improvements must justify the dramatic increase in construction cost. Also increasing the diameter of the tower and collector could be used to decrease the tower height.

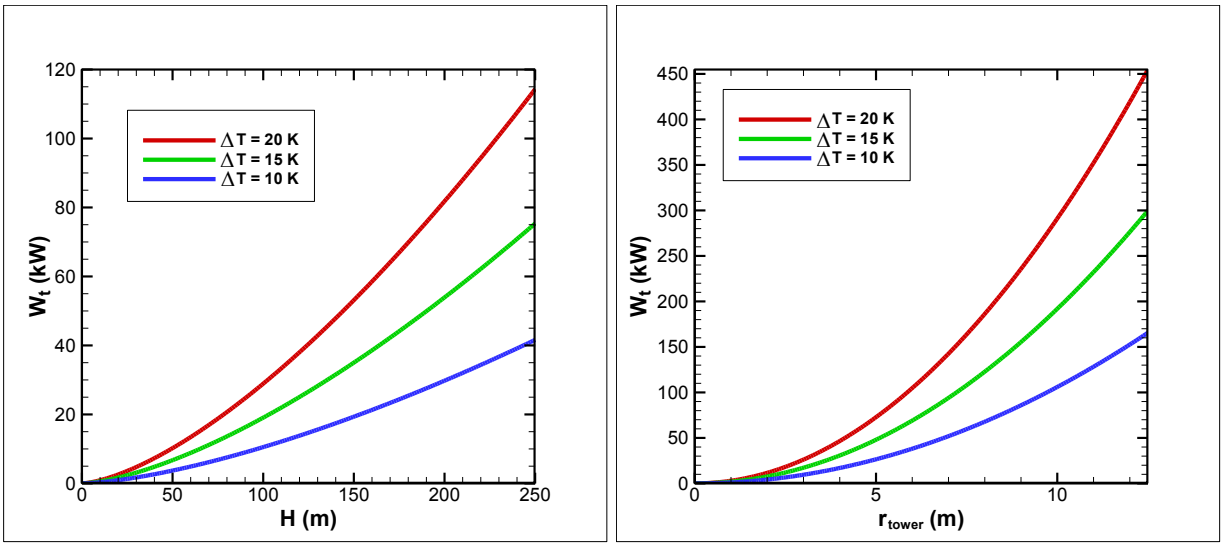

Figure 4.11: Maximum power output versus (a) height and (b) tower radius with a turbine load

4.7. Turbine Pressure Drop Investigation

Figure 4.12 presents the effects from varying the turbine pressure drop on the outlet vertical velocity, outlet temperature, and overall power output applying three different heat fluxes; 400, 500, and 600 W/m^2. These three cases are presented to compare the effects from altering the energy within the system. The pressure drop is varied, beginning with 0 Pa in increments of 40 Pa. The flow at the outlet is monitored to ensure the flow exits; once there is evidence that the flow tries to reverse direction at the outlet, the pressure drop is no longer varied. The power output is calculated using Equation (70) with the vertical velocities from the simulations. As the ground heat flux increases, the outlet velocity, outlet temperature, and power output all increase. Also, increasing the pressure drop decreases the outlet velocity and increases the outlet temperature. Increasing the pressure drop would significantly increase the overall power output of the system, however the power output has a parabolic shape. Thus there is a pressure drop that results in a maximum power output, and is consistent with Xu et al. [10].

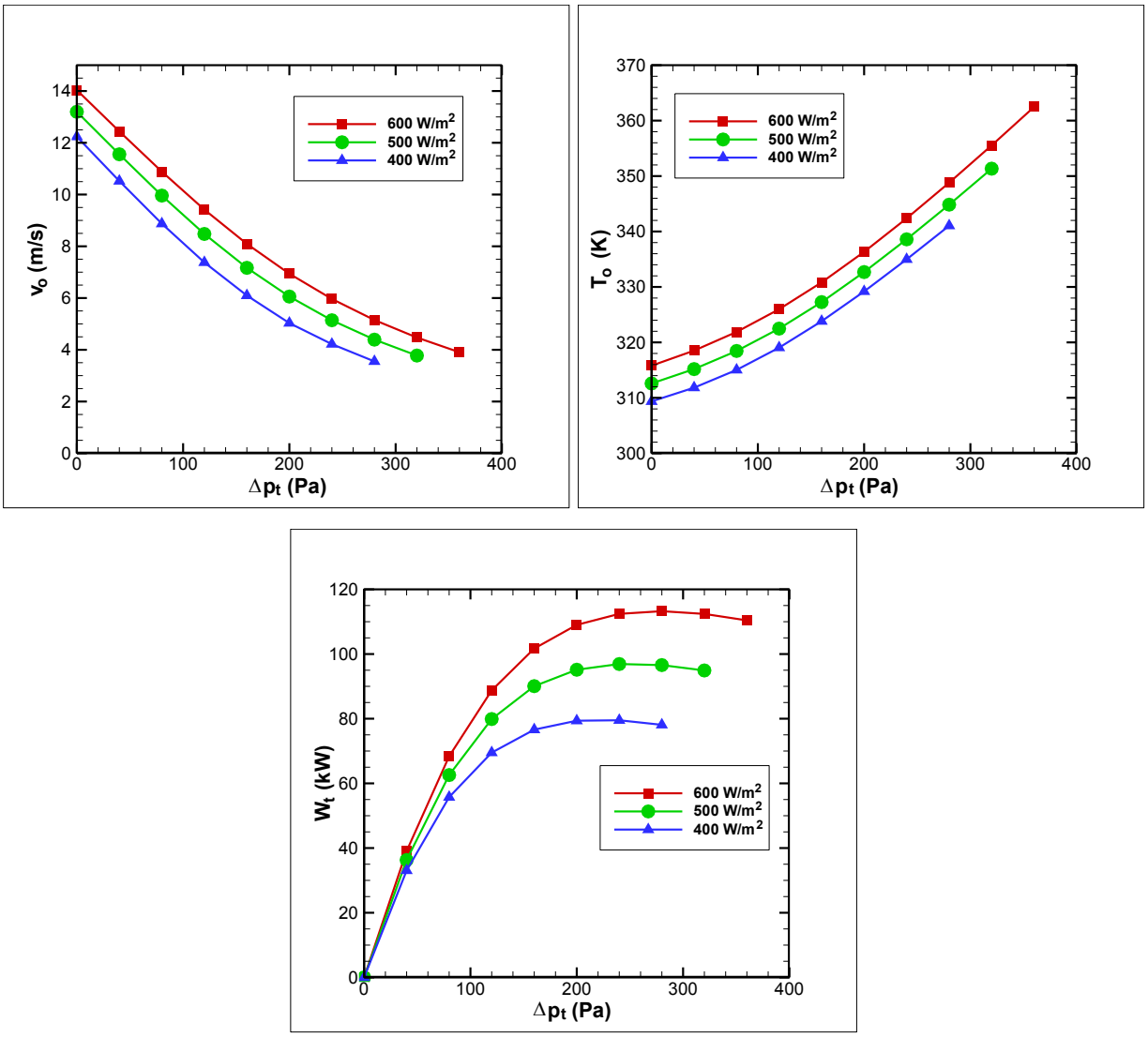

Figure 4.12: Outlet velocity, outlet temperature, and power output versus pressure drop for varying ground heat fluxes

The dimensionless variables for the pressure drop, outlet velocity, outlet temperature and power output are defined as:

$$\Delta p_t{}^* = \frac{\Delta p_t}{\rho \, v_o{}^2} \qquad (71)$$

$$v_o{}^* = \frac{v_o \, \rho_o \, L}{\mu_o} \qquad (72)$$

$$T_o{}^* = \frac{T_o - T_\infty}{T_H - T_\infty} \quad (73)$$

$$\dot{W}_t{}^* = \frac{\dot{W}_t}{\rho_o \, v_o{}^3} \quad (74)$$

The characteristic length, L, is defined as the diameter of the tower. The other parameters used to nondimensionalize are the outlet velocity, the air density, and the temperature T_H and T_∞. Figure 4.13 shows the nondimensionalized data first shown in Figure 4.12 for the outlet velocity and outlet temperature. Increasing the dimensionless pressure drop decreases the dimensionless outlet velocity and increases the dimensionless outlet temperature. The goal of applying the dimensionless variables is that the three curves from the different ground heat fluxes (Figure 4.12) collapse to a single curve. While the dimensionless outlet velocities from the three heat fluxes align onto a single curve, there is still some variance for the three dimensionless outlet temperature curves. A regression study is performed next using the four dimensionless equations from Equation (71) - (74).

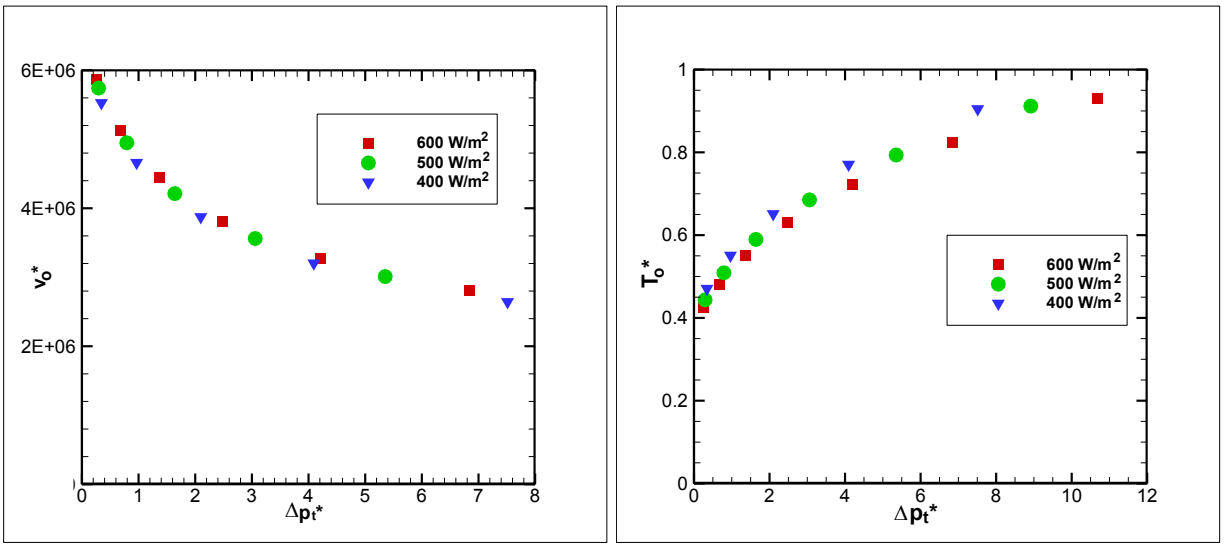

Figure 4.13: Dimensionless outlet velocity and temperature versus dimensionless turbine pressure drop

A regression study is performed to determine an equation that best fits the dimensionless parameters ($v_o{}^*$, $T_o{}^*$) to analytically determine the power output ($\dot{W}_t{}^*$). An equation of the form:

$$\dot{W}_{\mathrm{t}}{}^{*} = \mathrm{C}\, v_{\mathrm{o}}{}^{*\alpha}\, T_{\mathrm{o}}{}^{*\beta} \qquad (75)$$

The coefficients and exponents for the power output shown in Equation (75) are defined in Table 4.4. Also, Table 4.4 presents the *p*-value for each variable used in the regression analysis. The *p*-value represents the probability that the estimate would assume a greater value. Even though C has a high *p*-value, the term is still necessary because β has a *p*-value below 0.1. The regression has to be validated so that it successfully represents the dimensionless power output of the simulated solar chimney and can be used to predict the power output from the measured outlet vertical velocity and temperature.

Table 4.4: Regression parameter statistics

Variable	Estimate	*p*-Value
C	4210.78	0.9444
α	-0.568	0.4252
β	2.280	0.0618

Equation (75) and Table 4.4 show that increasing the dimensionless outlet temperature results in a higher power output and increasing the dimensionless outlet vertical velocity results in a lower power output. To validate the predictive equations, separate numerical cases are used. Table 4.5 presents the separate cases with the inputs (q_G" and Δp_t) and the resulting dimensionless variables. The predicted versus simulated power output for each case are compared in Figure 4.14.

Table 4.5: Other data used to validate regression equation

q_G'' (W/m)	Δp_t (Pa)	Δp_t^*	v_o^*	T_o^*
400	60	0.447	5494227	0.452
500	60	0.510	5341267	0.475
600	60	0.608	5087171	0.508
400	100	0.985	4778349	0.514
500	100	1.160	4572212	0.547
600	100	1.449	4255060	0.599
400	140	1.858	4117596	0.589
500	140	2.261	3875459	0.636
600	140	2.960	3523123	0.709

Figure 4.14 compares the simulated power output to the predicted power output for two sets of data: (a) the original data used to perform the regression and (b) the cases from Table 4.5 used to validate the regression. Ideally, the values should fall on the line, $y = x$, and both sets of data contain the desired trend. The variance of the regression calculated with part (a) is 0.991. The error bars are present in part (a) and represent the 95% single prediction intervals for the predicted values based on the numerical error using Mathematica. In addition, part (b) is magnified from 0 to 0.5 to show the dimensionless power output better. The data in part (b) aligns equally as well on the line y = x, so therefore, the regression represents the numerical data accurately. In conclusion, Equation (75) can be used to predict the power output of a simple solar power chimney.

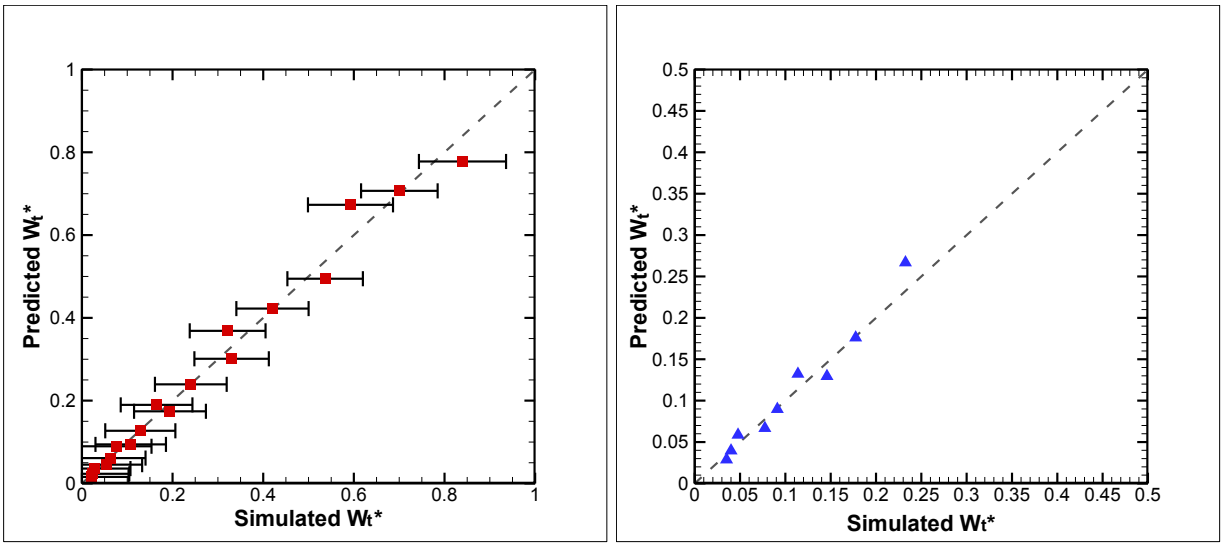

(a) (b)

Figure 4.14: Dimensionless power output; simulated versus prediction for data (a) used in the regression and (b) to verify regression analysis

Chapter 5. Conclusions and Recommendations

5.1. Conclusions

The growing consumption of energy and concerns for man-made climate change has motivated the desire for clean and reliable energy. In addition, providing energy to the rural Sub-Saharan Africa would greatly improve the lives of its inhabitants, especially in the evenings when villagers only have candle light to illuminate their homes. The solar chimney power plant provides clean reliable energy that would benefit locations that receive significant amounts of solar radiation. The focus of the study was to investigate the airflow and power output from the solar chimney system by developing a simplified numerical model with ANSYS Fluent.

Through three validation cases, the numerical methods and boundary conditions were investigated. The validation of a free plume investigated the solver types of pressure-based and density-based, the standard and realizable turbulence k-ε models, and the temporal discretization of first-order and second-order. The conclusion was that the pressure-based solver, realizable k-ε turbulence model, and first-order spatial discretization resulted in predictions more similar to that of Schaelin et al. [16] for a free plume. The second validation investigated the Rayleigh numbers effects on the flow and modeling a two-dimensional axisymmetric domain. Chergui et al. [13] and Tahar et al. [17] used similar modeling approaches but their conclusions were different for the Rayleigh number that resulted in the transition from laminar to turbulent flow. The current study concluded that the disagreement was the result of different definitions for the characteristic length; Chergui et al. [13] used the tower height, while Tahar et al. [17] used the average height of separation between the ground and solar collector. The final validation explored the boundary conditions for the turbine and the collector surface, and modeling the energy storage layer to represent the ground. Xu et al. [10] used a convection boundary condition for the collector and a

pressure drop for the turbine. The current study concluded that using a constant heat flux as the ground boundary condition allowed for a simpler geometry ignoring the energy storage layer.

The current study used a ground heat flux to create a numerical model of the solar chimney in Manzanares, Spain. The numerical model predicted similar values as the Spanish prototype measurements; therefore, the airflow and power output were investigated. The simulations showed that the inclusion of the turbine load increased temperatures and decreased velocities. It was shown that the flow through the tower did not significantly vary. These results are consistent with the known actual performance of a shrouded pressure-staged wind generator, which converts pressure into rotational energy [4]. As the air flows from the inlet towards the tower, the velocity and temperature increase. Also the inclusion of the turbine load results in higher pressures under the collector. It was also determined that the location of the turbine has little to no effect on the airflow and that the location should be determined from other factors such as safety, accessibility, etc.

An analytical equation for the turbine power output was developed to compare results with the numerical model. The first analytical equation defined the vertical velocity at the junction between the tower and collector without the turbine load. It was shown that the analytical solution compared well with the simulated and experimental data [15]. The second analytical equation defined the maximum power output from the system and the Betz power limit was also considered. The numerical predictions and experimental data were in-between the two power curves with and without the Betz limit. The analytical models were also used to investigate the effects of varying the geometry. Increasing the tower height or temperature within the system increased the vertical velocity. In addition, increasing either the tower diameter or height increased the power output of the turbine. The tower height had a more significant impact on the power output because the tower diameter also affects the temperature difference within the system.

The numerical model was used to investigate the effects of varying the turbine load. It was shown that there was a critical turbine pressure drop associated with a maximum power output, and further increasing the solar energy to the system increased this critical pressure drop. Key parameters (v_o and T_o) were nondimensionalized to demonstrate that the data for varying heat fluxes would collapse to a single curve. A regression study was performed to create a predictive equation for the useful work output. The predictive equation was tested for other random cases not used in the regression study. Additional simulations were performed and compared to the output using the prediction equation, demonstrating that the equation could be used for other chimney conditions.

5.2. Recommendations

Computational fluid dynamics is a vital numerical tool to research solar chimney power plants due to the extensive construction costs to build such large structures. A major goal of the current study was to replicate the prototype built in Manzanres, Spain with a simplified numerical model in ANSYS Fluent. The study can be continued by creating larger and/or more unique geometric configurations such as the solar chimney being designed by EnviroMission or implementing a wrapped tower of multiple shorter towers. The idea is that the sum of the heights of the shorter towers would equal the height of a single tower known to yield a desired energy output, e.g., 5-40 m tall towers would be equivalent to 1-200 m tower. In addition, the materials within the energy storage layer could be further investigated. Materials such as asphalt, water, etc. could be compared to soil material defined in Xu et al. [10]. Finally, the ability of harnessing the greenhouse effects by growing vegetation below the collector is a major benefit, so developing a numerical model accounting for the plant life below the collector would be another useful study.

The study also assumed steady-state flow and modeled the turbine with a user defined pressure drop, which allowed the power output to be calculated. A further study could be performed that develops a transient model representing a twenty-four hour cycle. The model would have to account for the different solar radiation values throughout the day and the turbine pressure drop would have to be an equation that varies vertical velocities. This transient model could be used to determine the amount of power generated at individual times throughout the day, which would benefit the electrical management of the village.

The current study also investigated analytical models for the power output of the system. In these equations, the efficiencies of the tower and collector were defined, but the efficiency of the turbine for the Spanish prototype was assumed to be 0.8 from an estimation from Haaf et al. [15]. Further investigating the calculations for the turbine efficiency would strengthen the analytical models. The diameter could possibly impact the turbine efficiency and/or pressure drop due to the tower radius being equal to the lengths of the blades. In addition, developing an equation for turbine efficiency would allow for a better understanding of both altering the geometry of the solar chimney and changing the location of the turbine. For example, the current study concluded that the placement of the turbine had insignificant impact on the overall power output, but a calculation could provide more insight on the differences between one larger turbine at the base of the tower and many smaller turbines below the collector.

Finally, the predictive equation can be expanded with more numerical cases that vary the collector radius along with the tower height and radius. Using these new cases, a predictive equation can be developed such that the equation could present the effects from the geometry. The current study created a predictive equation that represents the flow within a solar chimney with the same dimensions of the prototype built in Spain, and an updated equation would be beneficial.

Hopefully, research of solar chimney power plants continues to advance so that an optimal tower can designed and then built in Sub-Saharan Africa to provide reliable electricity to the inhabitants. This thesis explored the airflow within the solar chimney and modeled the turbine so that the power output could be calculated, but there is much more CFD research to be performed on the subject before they become a worldwide source of power. The prototype in Manzanares, Spain proved that the idea was viable and that solar updraft towers can be a leading energy provider in many areas.

References

[1] Dhari, A., and Omri, A., 2013, "A Review of solar Chimney Power Generation Technology," International Journal of Engineering and Advanced Technology, 2(3), pp. 1-17.

[2] Grose, T. K., 2014, "Solar Chineys Can Convert Hot Air to Energy, But is Funding a Mirage?," Online, http://news.nationalgeographic.com/news/energy/2014/04/140416-solar-updraft-towers-convert-hot-air-to-energy/.

[3] "Technology Overview," http://www.enviromission.com.au/EVM/content/technology technologyover.html.

[4] Schlaich, J., 1996, The Solar Chimney, Edition Axel Menges

[5] Humphries, M., 2011, "Solar Tower in Arizona to power 150,000 homes for 80 years," Online, http://www.geek.com/geek-pick/solar-tower-in-arizona-to-power-150000-homes-for-80-years-1406459/.

[6] 2013, "Power Africa," http://www.usaid.gov/powerafrica.

[7] 2015, "SolarGIS," Online, http://solargis.info/doc/free-solar-radiation-maps-GHI.

[8] Wolf, M. I., 2008, "Solar Updraft Towers: Their Role in Remote On-Site Generation," MIT.

[9] Pastohr, H., Kornadt, O., and Gurlebeck, K., 2004, "Numerical Analytical Calculations of the Temperature Flow Field in the Upwind Power Plant," International Journal of Energy Research(28), pp. 495-510.

[10] Xu, G., Ming, T., Pan, Y., Meng, F., and Zhou, C., 2010, "Numerical Analysis of the Performance of solar chimney Power Plant System," Energy Conservation and Managment(52), pp. 876-883.

[11] Ming, T., Liu, W., Pan, Y., and Xu, G., 2008, "Numerical Analysis of Flow and Heat Transfer Characteristics in Solar Chimney Power Plant with Energy Storage Layer," Energy Conversion and Managment(49), pp. 2872 - 2879.

[12] Fasel, H. F., Meng, F., Shams, E., and Gross, A., 2013, "CFD Analysis for Solar Chimney Power Plants," Solar Energy(98), pp. 12 - 22.

[13] Chergui, T., Larbi, S., and Bouhdjar, A., 2010, "Thermo-hydrodynamic aspect Analysis of Flows in Solar Chimney Power Plants-A Case Study," Renewable and Sustainable Energy Reivews(14), pp. 1410 - 1418.

[14] Tahar, T., and Mahfoud, D., 2012, "Numerical Simulation of Natural Convection in a Solar Chimney," International Journal of Renewable Eneregy Research, 2(4), pp. 712-717.

[15] W. Haaf, K. F., G. Mayr, and J. Schlaich, 1883, "Solar Chimneys, Part I: Principle and Contruction of the Pilot Plant in Manzanares," Solar Energy, 2, pp. 3-20.

[16] Schaelin, A., Maas, J. v. d., and Moser, A., 1992, "Simulation of Airflow Through Large Openings in Buildings," The American Society of Heating, Refrigerating, and Air-Conditioning Engineers, Inc.Baltimore, Maryland, pp. 317-328.

[17] Tahar, T., and Mahfoud, D., 2013, "Numerical Analysis of Flows in a Solar Chimney Power Plant with a Curved Junction," International Journal of Energy Science, 3(4), pp. 280-286.

[18] "FLUENT 15.0 User's Guide," Ansys Incorporated.

[19] Ismail B. Celik, U. G., Patrick J. Roche, Chrisotpher J. Frietas, Hugh Coleman, and Peter E. Raad, 2008, "Procedure for Estimation and Reporting of Uncertainty Due to Discretization in CFD Applications," Journal of Fluids Engineering, 130.

[20] Dewitt, F. I. a. D., 2002, Fundamentals of Heat and Mass Transfer, John Wiley & Sons, Inc.

[21] Alnaser, W. F., 1989, "Estimation of the Clear Sky and the Ground Emissivity in Bahrain," Earth, Moon, and Planets, 48, pp. 177-181.